Towards Efficient Aerodynamic and Aeroacoustic Optimization for Urban Air Mobility Vehicle Design

Bernardo Pacini[1], Anil Yildirim[2], Behdad Davoudi[3], Joaquim R. R. A. Martins[4], and Karthik Duraisamy[5]
University of Michigan, Ann Arbor, MI, 48109

Abstract

Urban air mobility vehicles have taken form as advanced rotorcraft with sets of wings, rotors, canards, and other appendages. Noise generation is an important technical barrier that must be addressed to prevent these vehicles from causing excessive disturbance to the communities they are intended to service. There is a need for efficient and low-fidelity analysis tools specifically for the conceptual design and sizing phase of urban air mobility vehicle development. Such tools must be computationally efficient to allow for repeated analyses needed for design optimization. This paper presents coupled aerodynamic and aeroacoustic analysis formulated for gradient-based design optimization. Rotor performance is modeled using HELIX, a hybrid blade element momentum theory tool, coupled with PULSE, an aeroacoustic analysis tool based on the Ffowcs Williams and Hawkings aeroacoustic analogy, reformulated as Farassat Formulation 1A. This work presents a methodology for computing implicit derivatives of the coupled aerodynamic and aeroacoustic models implemented within the software package OpenMDAO. Both models are validated independently, and derivatives are verified using finite difference and complex step approximations. These tools are used to analyze and optimize the rotors on the single passenger NASA N+1 quadrotor vehicle with respect to blade-shape parameters. This paper aims to introduce aeroacoustic analysis into gradient-based optimization efficiently and demonstrate the impact that such optimization can have for minimizing the noise footprint of an urban air mobility vehicle.

1 Introduction

Urban air mobility (UAM) is an emerging market that aims to improve transportation networks in urban and rural environments utilizing advanced aerial vehicles [1]. Vehicles designed for UAM aim to provide efficient travel for both faster and further transportation [2]. Currently, many cities across the globe face congestion challenges as their highway systems are unable to cope with the increased number of residents and daily commuters. Similarly, many rural areas have become secluded as they are out of reach of convenient travel from large residential centers [2]. By developing vertical or short takeoff and landing vehicles, an entirely new type of transportation can be created, improving the connectivity and efficiency of transportation systems. UAM vehicles have taken shape as complex rotorcraft with sets of propellers, rotors, wings, canards, and other appendages. These vehicles have become possible due to the convergence of many technologies, including electric propulsion and autonomous flight systems [1, 3]. While some UAM prototypes have been tested extensively, their community acceptance remains unknown.

NASA has identified ten areas of technological development necessary for UAM deployment on a large scale. These areas range from ease of certification to efficiency to community noise and annoyance [1, 4]. Vehicle noise generation is a critical technological barrier that must be addressed to make UAM feasible. If a noise limit is not achieved, communities will likely deem UAM infeasible as it will be too disruptive [2, 4]. To promote technology development, NASA released reference vehicles, known as the N+1 vehicle designs [4]. These vehicles include a one-person electric quadrotor, a six-person side-by-side helicopter with hybrid propulsion, and a fifteen-person tiltwing turboelectric vehicle [4]. A lift+cruise vehicle was added to the N+1 designs as an additional research vehicle [5, 6]. All of the vehicles were designed using multidisciplinary analyses with comprehensive vehicle design tools; however, acoustic performance was not directly included as a consideration. Instead, the vehicles were designed to maintain a low rotor tip speed to reduce noise, and rotors were placed in ways that decrease the likelihood of noisy blade-to-blade and rotor-to-rotor interaction. A study on developments of electric propulsion for aircraft found that electric aircraft design is likely to be a highly coupled problem between disciplines, meaning it is important to incorporate relevant vehicle design and performance analyses in a complete vehicle design optimization framework [7]. Furthermore, noise generation is largely determined in the conceptual design phase [2], suggesting that careful multidisciplinary design optimization throughout the preliminary design optimization process can help reduce vehicle noise.

A frequently used method for rotor performance modeling is blade element momentum theory (BEMT), which provides an efficient technique for computing rotor performance and blade loading by combining momentum analysis with blade element analysis [8]. While accurate for axial flow scenarios, many BEMT formulations are unable to predict rotor performance in off-axial or edgewise flight accurately. This limitation poses a significant restriction limiting the method's usability for many new vehicle designs, such as edgewise flight quadrotors. To improve BEMT's versatility, novel hybrid blade element momentum theory (HBEM) methods have been proposed, combining blade element analysis and momentum theory in a way that allows for forward flight analysis [9, 10]. One such method is particularly useful for vehicle control applications, using parameter fitting to identify aerodynamic parameters for a specific vehicle in question [9]. A more general formulation uses blade geometry and flight conditions to iteratively identify the relationship between forces and moments and a rotor's angular velocity [10]. This methodology is general and provides a useful technique for efficient rotor design analyses needed for optimization studies. Unfortunately, BEMT methods, including HBEM, offer poor robustness, making them challenging to use for repeated design optimization analyses. To combat this issue, the underlying formulation and iterative solving techniques can be adapted to provide a formulation that guarantees a solution [11]. This robust methodology has been successfully used for wind turbine optimization studies, ensuring efficient and guaranteed solutions at each design iteration [12].

Using a robust solution method for rotor performance and blade loads, the aeroacoustic footprint of a rotor can be computed to quantify the noise it generates in flight. A commonly used method for rotorcraft aeroacoustic modeling is the Ffowcs Williams and Hawkings model (FWH) [13]. This model is an integral-based formulation that is a direct refactoring of the Navier-Stokes equations and has shown to be a useful tool specifically for rotor analysis [14]. The Farassat Formulation 1A is a simplified variant of the FWH model that can be efficiently implemented within computational tools to obtain noise measurements with varying degrees of fidelity [15]. This formulation has been used for several UAM noise generation studies, such as investigating the acoustic performance of electric, low-tip-speed propellers [16]. Further studies have investigated the validity of using such methods, typically implemented for helicopters, for modern rotorcraft featuring sets of rotors, wings, and other appendages [17–19]. While self-noise appears to be an increasingly important noise source, especially at low Reynolds numbers, these studies found that the FWH model, formulated as Farassat Formulation 1A can accurately predict noise generation for small unmanned aerial vehicles. Furthermore, similar studies investigated the effects of different vehicle and rotor configurations, such as the use of stacked, co-rotating rotors [20]. Understanding model accuracy and vehicle noise sources is an ongoing research area that is important for vehicle design and optimization studies.

Performing multidisciplinary design optimization is likely an important aspect of electric vehicle design, given the close-coupling between vehicle components [7]. Such optimization studies can be carried out using the software package OpenMDAO, a framework for design problems with underlying coupled numerical models [21]. OpenMDAO offers efficient techniques for computing problem derivatives, such as the direct or adjoint methods [22, 23], and provides tools for interfacing with gradient-based optimizers to define and optimize a vehicle design. This framework has been used successfully for aeroacoustic optimization, for example, for optimizing the trajectory of a vehicle using a simplified monopole noise source [24]. Further work on electric vehicles using OpenMDAO found that the traditional design process was not able to comprehensively analyze the interdisciplinary environment defining a UAM vehicle [25, 26]. Model coupling, analysis, and optimization using OpenMDAO proved to be important for understanding and optimizing UAM vehicle concepts and has been used for further optimization analyses, incorporating aeroacoustic considerations [27, 28].

In this paper, we present a set of techniques, coupled using OpenMDAO, to perform gradient-based multidisciplinary design optimization of a NASA N+1 UAM vehicle. The aerodynamic and rotor performance modeling is carried out using a quasi-steady HBEM model, formulated to be used with the direct implicit derivative computation method. This model is used to compute rotor blade loads as well as rotor performance, such as total thrust and coefficient of thrust. The results from the HBEM model are passed through OpenMDAO to an aeroacoustic analysis tool based on the Farassat Formulation 1A. The coupled models are differentiated using forward-mode algorithmic differentiation, and derivatives are verified with both the finite difference and complex step derivate computation techniques. The goal of this paper is to showcase an efficient methodology for aeroacoustic-informed rotor optimization, leveraging quasi-steady assumptions to help improve the efficiency of time-accurate optimization analysis.

2 Computational Methods

Coupled aerodynamic and aeroacoustic optimization can be carried out by combining both disciplines within a multidisciplinary design optimization framework. In this work, aerodynamic and aeroacoustic analysis tools are combined within the framework OpenMDAO, which handles data passage and coupled gradient computation for gradient-based optimization. The structure of the optimization problem is presented in an extended design structure matrix (XDSM) [29] diagram in Figure 1.

The optimization workflow follows the black arrows, whereas the gray lines signify data passing between components, such as geometry or ambient flow parameters. Parameters that are case-specific and not solution states are denoted as x_i, and are passed as needed to specific components within the framework. Each optimization cycle begins by solving for the aerodynamic state of the flow, in this case focusing on rotor performance using a BEMT model. This nonlinear block, denoted Aerodynamic Analysis, is converged using a nonlinear solver to decrease the residual, $\mathcal{R}(u_1)$, to zero. The state variable, u_1, is the aerodynamic solution state, while u_2 is the aerodynamic data required for aeroacoustic analysis. Once the aerodynamic solver is converged, both the aerodynamic solution state and additional data are passed to the Aeroacoustic Analysis block. This block does not require a solver, as it acts as a post-processor for the aerodynamic data. The results from the aerodynamic and aeroacoustic analysis are passed to the Functional Evaluations block, where quantities of interest are computed. These quantities are values of interest such as noise level or rotor thrust and are returned to the optimizer in the form of an objective function, f, and constraint function, c values. All state variables in the figure appear as stacks because the analyses are inherently time-accurate; that is, the variables represent time-histories of aerodynamic and aeroacoustic quantities. The workflow is repeated for each optimization iteration, following the path described by the black arrows.

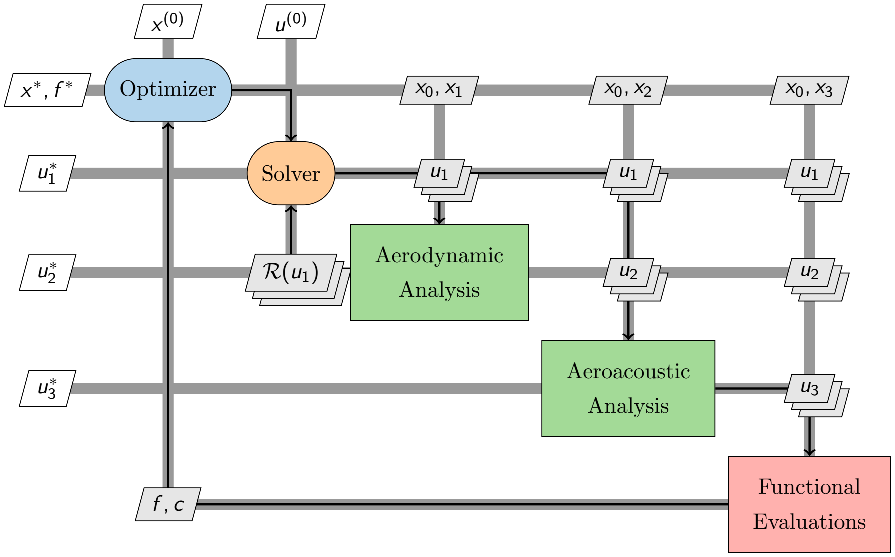

Figure 1: eXtended Design Structure Matrix (XDSM) for coupled aerodynamic-aeroacoustic optimization. Optimization iterations follow the black arrows and additional data passes through the gray lines. Variables denoted with x_i are design variables and case parameters, variables denoted with u_i are state variables, and f and c are the objective and constraint function values, respectively.

2.1 Aerodynamic Modeling

BEMT is a popular and computationally efficient approach for modeling rotor aerodynamic performance [8]. Using BEMT for UAM aeroacoustic informed optimization has been investigated [27] and has shown promise using reduced-fidelity tools with simplifying assumptions. However, many BEMT models impose restrictions on the flight scenarios that can be modeled, such as allowing for only axial free-stream flow. HBEM, formulated in this work within a tool called HELIX, is an extension of BEMT that has been developed to handle a variety of flight scenarios beyond axial flight [10]. This is a useful tool for vehicle design as it can be applied to configurations that fly in neither fully edgewise flight nor fully axial flight. Similarly, as compared to traditional BEMT methods such as the ones employed in [27], HBEM is not restricted to azimuthal symmetry. This is a particularly important consideration for aeroacoustic analysis as transient loading effects can yield substantial variations in noise generation.

BEMT relies on a combination of blade element theory and momentum theory. Momentum theory, depicted in Figure 2a, assumes a rotor operates as a disk, encased within a streamtube. This streamtube contracts as the disk accelerates the flow, generating thrust. As opposed to momentum theory, where a rotor's geometry is not needed, blade element theory is a technique for computing rotor performance by analyzing blade sections. As shown in Figure 2b, airfoil properties and flow conditions are used to compute the lift, thrust, and drag generated by individual blade sections. This analysis depends on the rotor inflow velocity at the location in question, $\phi(r)$, the element twist, θ_0, and blade properties such as the airfoil lift-curve-slope. By discretizing a single rotor revolution about its azimuthal axis, blade element theory can be used to compute the total thrust a rotor generates. BEMT is based on the combination of momentum theory and blade element theory, using aspects of both methods to compute rotor performance.

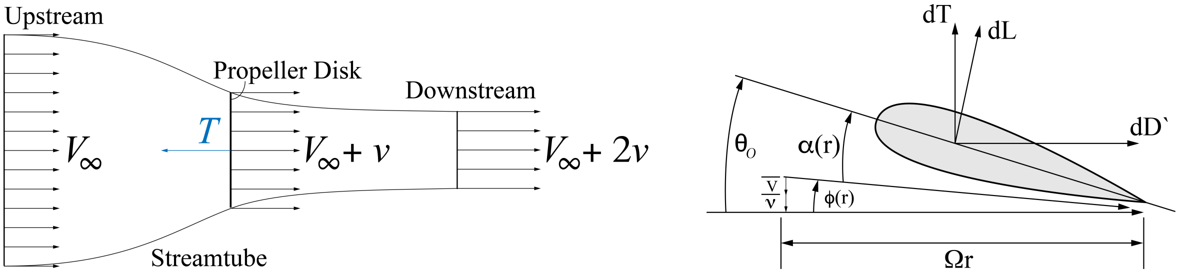

(a)

(b)

Figure 2: Schematics for blade element momentum theory (a) momentum theory streamtube with propeller disk (b) blade element theory element cross section

HBEM is based on the requirement that momentum theory and blade element theory yield the same thrust coefficient over one rotor revolution. The thrust coefficient calculated with momentum theory ($C_{T,MT}$) can be computed using the desired rotor thrust T_{des}, radius R, and tip speed V_t, along with free-stream density ρ_0. This can be written as:

$$C_{T,MT} = \frac{T_{\text{des}}}{\pi \rho_0 V_t^2 R^2}. \tag{1}$$

In contrast to momentum theory, blade element theory accounts for blade geometry and requires time-marching through one rotor revolution. A linear inflow model for blade element theory can be written to describe the flow entering and passing through the propeller disk area [8],

$$\lambda = \lambda_0 \left(1 + k_x r \cos(\psi) + k_y r \sin(\psi)\right), \tag{2}$$

where λ_0 is the uniform inflow ratio and can be obtained as an extension of momentum theory, k_x and k_y are model-based parameters that are problem dependent, r is the radial location along the rotor blade, and ψ is the azimuthal angle of rotation. The inflow ratio is then used to define the radial (u_r), tangential (u_t), and perpendicular (u_p) velocity components passing over the rotor:

$$u_r = \mu \cos(\psi); \quad u_t = r + \mu \sin(\psi); \quad u_p = \lambda. \tag{3}$$

An initial evaluation of the lift generated by each discretized rotor section can be computed using a blade section's lift-curve-slope, C_{l_α}, and effective angle of attack α_{eff}.

$$C_l = C_{l_\alpha} \alpha_{\text{eff}}, \tag{4}$$

where $\alpha_{\text{eff}} = (\theta_0 - \alpha_{l=0} - \phi)$. θ_0 represents the angle of attack of the blade section, $\alpha_{l=0}$ is the angle of attack of zero-lift, and ϕ is based on the velocity of the incoming flow as $\phi = \tan^{-1}(u_p/u_t)$. A stall model is applied to the lift coefficient calculation to improve this approach's fidelity and avoid having the optimizer exploit unphysical angles of attack [30]. This model adjusts the computed coefficient of lift based on an effective angle of attack, using the airfoil stall transition angle α_0, and transition parameter M. The modified coefficient of lift equation is reformulated as

$$C_l = (1-\sigma)C_{l_\alpha}\alpha_{\text{eff}} + \sigma[2sign(\alpha_{\text{eff}} - \alpha_{L=0})\sin^2(\alpha_{\text{eff}} - \alpha_{L=0})\cos(\alpha_{\text{eff}} - \alpha_{L=0})], \quad (5)$$

where

$$\sigma = \frac{1 + e^{-M(\alpha_{\text{eff}} - \alpha_{L=0} - \alpha_0)} + e^{M(\alpha_{\text{eff}} - \alpha_{L=0} + \alpha_0)}}{\left[1 + e^{-M(\alpha_{\text{eff}} - \alpha_{L=0} - \alpha_0)}\right]\left[1 + e^{-M(\alpha_{\text{eff}} - \alpha_{L=0} + \alpha_0)}\right]}. \quad (6)$$

Ultimately the coefficient of thrust for blade element theory can be computed as:

$$C_{T,BET} = \frac{N_b}{4R^2\pi^2}\int_0^R\int_0^{2\pi} C_l u^2 c(r)\cos(\phi)d\psi dr. \quad (7)$$

Here N_b is the number of blades on the rotor, $c(r)$ is the chord length of the blade as a function of rotor radius, and u is the magnitude of velocity at the simulated blade section: $u = \sqrt{u_p^2 + u_t^2}$. For the application in this paper, rotor thrust is solved iteratively to satisfy the requirement that momentum theory and blade element theory yield the same thrust coefficients. The residual for this iterative solver procedure can be written formally as

$$\mathcal{R}(T_{mag}) = C_{T,BET}(T_{mag}) - C_{T,MT}(T_{mag}), \quad (8)$$

where the state variable, T_{mag}, is the magnitude of the thrust of the rotor at each time-step. Momentum theory and blade element theory are computed, and the residual is converged for each time-step and each rotor, yielding a quasi-steady analysis that can be used for aeroacoustic analysis. To ensure robust convergence, a line search method is used to identify a region that contains the solution to the system. Then, a solution is found using Brent's method, a root-finding algorithm with guaranteed convergence [31].

This methodology is implemented within an analysis tool called HELIX that simulates quasi-steady rotor performance. HELIX is written for coupling with aeroacoustic analysis and outputs both rotor performance such as rotor thrust, torque, and moment coefficients, as well as time-accurate blade loads. The HBEM formulation used within HELIX captures the foundation of BEMT but does not include advanced corrections such as root and tip loss models. Adding such models to HELIX can improve the fidelity of the results while incurring a computational cost. Within the present work, HELIX is used to compute rotor thrust and blade loads that are used for aeroacoustic analysis.

2.2 Aeroacoustic Modeling

Formulations for computing noise generated by a moving surface can be derived from the Navier–Stokes equations governing fluid dynamics. These models require close coupling with aerodynamic solvers, as time histories of each of the aerodynamic state variables are needed to accurately compute noise generation. One integral-based formulation for aeroacoustic analysis is the FWH model, which computes monopole, dipole, and quadrupole noise sources [13]:

$$4\pi a_0^2 \rho' = \underbrace{\frac{\partial^2}{\partial x_i \partial x_j}\int_V \frac{HT_{ij}}{r\|1-M_r\|} d^3\eta}_{\text{Quadrupole}} - \underbrace{\frac{\partial}{\partial x_i}\int_S \frac{P_{ij}+\rho_0 v_i(v_j-u_j)}{r\|1-M_r\|} n_j dS(\eta)}_{\text{Dipole}} + \underbrace{\frac{\partial}{\partial t}\int_S \frac{\rho_0 u_i + \rho_0(v_i-u_i)}{r\|1-M_r\|} n_i dS(\eta)}_{\text{Monopole}}. \tag{9}$$

The quadrupole noise term is particularly challenging to compute but is generally considered less significant than the dipole and monopole terms, particularly at low tip Mach numbers. For this study, the quadrupole noise term is not considered in the noise calculation. Several reformulations of the FWH model have been suggested and one commonly used variant is Farassat Formulation 1A [15], which transforms the dipole and monopole pressure perturbation terms into integrals for loading (p'_L) and thickness (p'_T) pressure perturbations, written as

$$p'_L(\vec{x},t) = \frac{1}{4\pi a_0}\int_S \left[\frac{\dot{F}_i \hat{r}_i}{r(1-M_r)^2}\right]\Bigg|_{\tau*} dS + \frac{1}{4\pi}\int_S \left[\frac{F_i(\hat{r}_i - M_i)}{r^2(1-M_r)^2}\right]\Bigg|_{\tau*} dS + \frac{1}{4\pi a_0}\int_S \left[\frac{F_i \hat{r}_i (r\dot{M}_i \hat{r}_i + a_0(M_i \hat{r}_i - M_i M_i))}{r^2(1-M_r)^3}\right]\Bigg|_{\tau*} dS \tag{10}$$

$$p'_T(\vec{x},t) = \frac{1}{4\pi}\int_S \left[\frac{\rho_0 \dot{u_n}}{r(1-M_r)^2}\right]\Bigg|_{\tau*} dS + \frac{1}{4\pi}\int_S \left[\frac{\rho_0 u_n (r\dot{M}_i \hat{r}_i + a_0(M_i \hat{r}_i - M_i M_i))}{r^2(1-M_r)^3}\right]\Bigg|_{\tau*} dS. \tag{11}$$

These equations depend on the force on the blade, F, and its derivative in time, the component directions of the Mach number of each geometry panel, M_i, the velocity components of the panels, u_i, and the free-stream density ρ_0 and speed of sound a_0. This blade data is passed from a coupled aerodynamic analysis, such as from the HBEM model. As shown in Figure 3, the blade data is radiated outwards to a desired observer point location to compute retarded time, τ^*. This represents the time at which a particular set of blade element data reaches the observer point computed as a pressure perturbation. The retarded time is interpolated to the desired observer time vector and used to compute the blade element location, velocity, forcing, and area in source time. This interpolation is done using Akima interpolation to smooth the input time-history data [32]. Once data has been interpolated to the required source time for each observer, the dipole and monopole pressure perturbation contributions can be computed at each observer point.

This formulation assumes an accurate rotor geometrical representation, in particular to compute monopole noise. Monopole noise is based on rotor geometry and cannot be modeled directly using Farassat Formulation 1A with simplifying approximations such as blade-element modeling. An alternative technique for modeling monopole noise can be implemented using sets of sources and sinks positioned at locations along defined element sections [33]. These chordwise sections provide a reduced-fidelity model

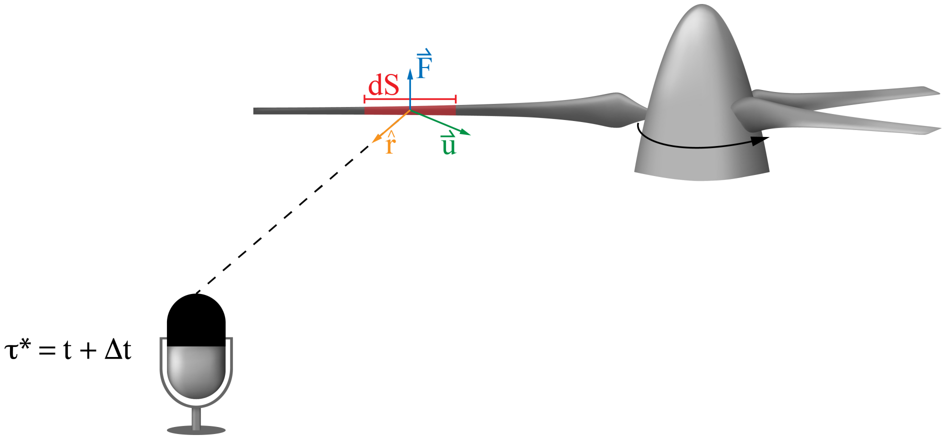

Figure 3: Schematic of a rotor blade section, approximated as a source surface for Farassat Formulation 1A. Element data is propagated to an observer point of interest to compute the pressure perturbation in retarded time.

to compute monopole noise, even when blade-element model assumptions are made. This technique is implemented within a computational aeroacoustic analysis tool as a compact aeroacoustic formulation, allowing for efficient analysis of monopole noise sources.

Sound pressure level represents the total noise of a pressure perturbation time history, serving as a useful metric for quantifying the impact of aeroacoustic noise. Sound pressure level is computed by comparing the root mean square of the pressure time history to a reference pressure, taken as $p_{\text{ref}} = 2 \times 10^{-5}$ Pa,

$$\text{SPL} = 20 \log_{10} \frac{p_{\text{rms}}}{p_{\text{ref}}}. \tag{12}$$

Given aerodynamic loading data, Farassat Formulation 1A, with a compact monopole noise model, is able to compute tonal noise generated by a vehicle in flight [34], but does not capture noise such as high-speed impulsive noise or broadband noise. These sources are not considered within the present work; however, broadband noise may significantly contribute to aeroacoustic noise in low tip-speed UAM vehicles. For this work, Farassat Formulation 1A with a compact monopole noise model is implemented within an analysis tool called PULSE and used to compute the noise on a plane of observer points below a UAM vehicle in hover flight condition.

2.3 Multidisciplinary Design Optimization Coupling

Gradient-based optimization can substantially improve optimization performance, as compared to gradient-free methods [35]. To perform gradient-based optimization, the gradients of the objective function and all constraints with respect to the design variables must be computed. This means that the aerodynamic analysis, the aeroacoustic analysis, and the functional evaluations must be differentiated or these derivatives must be approximated using derivative computation techniques such as finite difference or complex step [36]. The gradients of interest can be written as:

$$\frac{df}{d\mathbf{x}} : \text{Objective Function Gradient} \qquad \frac{d\mathbf{c}}{d\mathbf{x}} : \text{Constraint Functions Gradients}$$

In this notation, f is the objective function, computed as a scalar value, while $\mathbf{x}$ and $\mathbf{c}$ are vector quantities representing the design variable vector and vectorized constraints, respectively. The dimensions of these matrices are dependent on the number of design variables and constraint functions. The gradients of the objective function ($df/d\mathbf{x}$) form a vector with a length of number of design variables (n_x). Instead, the gradients of the constraints ($d\mathbf{c}/d\mathbf{x}$) form a matrix with dimensions n_c by n_x, or number of design variables by number of constraints.

The values for the required gradients can be computed in various ways, ranging in implementation difficulty, computational effort, and memory usage [23]. The most straightforward way of computing a derivative is to use the finite difference method. This method is non-intrusive; it approximates the derivatives by computing the relative change in functions of interest after perturbing one design variable at a time. The first-order forward finite difference scheme for the objective function derivative with respect to the ith design variable (x_i) can be written as

$$\frac{df}{dx_i} = \frac{f(x + \Delta x_i) - f(x)}{\Delta x_i}. \tag{13}$$

This method is useful as it has a low implementation cost and can be used to compute gradients across an entire system without having to consider the intricate details involved in coupled analysis. However, finite difference methods suffer from noisy derivatives that can make optimizations challenging to converge. Decreasing the step size, Δx_i, improves the finite difference approximation to a point until numerical precision errors become dominant and the finite difference approximation becomes inaccurate. When working with finite differences, the step size must be carefully chosen to correctly compute gradients, making it challenging to use reliably [23]. Additionally, the cost of computing gradients using finite differences is tied to the number of design variables. The entire system, including iterative solutions and model couplings, must be computed for each design variable gradient computation.

An alternative to using finite differences is the complex step method [36]. This approach follows a similar procedure to the finite difference method; however, the perturbation on the variable of interest is taken in the imaginary direction. The formula for the complex step derivative of the objective function with respect to a design variable, x_i, can be written as

$$\frac{df}{dx_i} = \frac{\mathrm{Im}\left[f(x + i\Delta x_i)\right]}{\Delta x_i}. \tag{14}$$

The complex step method does not suffer from numerical cancellation issues, as there is no subtractive operation in the equation. Consequently, the step size can be made extremely small, limited by numerical precision, to compute derivatives with numerical precision accuracy. This method is more difficult to implement than finite difference because the source code for each analysis component must be compatible with complex numbers, and necessary code operations must be overloaded to ensure accurate derivatives [36]. Source code transformation and operator overloading can be challenging to implement accurately. This method is advantageous as it can be used across coupled models without advanced model coupling techniques and yields gradients that are accurate to numerical precision. However, this method also requires a higher computational effort as the computations are more complicated than the finite difference method. As with the finite difference method, the complex step method cost scales with the number of design variables. The entire system, including iterative solutions and model couplings, must be computed for each design variable derivative computation, taking care that the imaginary components in iterative solvers converge to necessary tolerances.

An alternative method to finite difference and complex step methods is algorithmic differentiation (AD), where source code is parsed and re-written with additional lines for derivative computation. Forward-mode AD is similar to the finite difference and complex step methods because it finds the gradients of all output values with respect to a single design variable of interest. As with the finite difference and complex step, the code can be run repeatedly, once for each design variable, to find all the derivatives of design variables. Conversely, reverse-mode AD computes derivatives of a single output value, computing all of the gradients of a single output value with respect to all of the design variables of interest. This method is particularly advantageous when the number of outputs, $n_f + n_c$, is notably less than the number of inputs, n_x. Directly computing gradients from an algorithmically differentiated code requires repeatedly solving the governing equations in the model, which is often an iterative and inefficient task.

Implicit analytic methods are a set of techniques that avoid converging governing equations repeatedly when computing derivatives, improving the efficiency of derivative computation [22, 37]. When computing derivatives of a model with an implicit component, such as an iterative solver, the functions of interest depend on both the design variables and solution state variables. The function of interest and residual of the governing equation can be written explicitly as:

$$f = f(\mathbf{x}, \mathbf{u}(\mathbf{x})) : \text{Function of Interest} \qquad \mathcal{R}\left(\mathbf{x}, \mathbf{u}(\mathbf{x})\right) = 0 : \text{Solution Residuals} \tag{15}$$

By using the chain rule, the total derivative of a single function of interest can be written as

$$\underbrace{\frac{df}{d\mathbf{x}}}_{1 \times n_x} = \underbrace{\frac{\partial f}{\partial \mathbf{x}}}_{n_f \times n_x} + \underbrace{\frac{\partial f}{\partial \mathbf{u}}}_{1 \times n_u} \underbrace{\frac{d\mathbf{u}}{d\mathbf{x}}}_{n_u \times n_x}, \tag{16}$$

where the total derivatives, denoted by $d(\cdot)/d(\cdot)$ require converging the governing equations, while partial derivatives, denoted by $\partial(\cdot)/\partial(\cdot)$ do not. A similar expansion can be applied to the residual equation, forcing the system to equal zero as the governing equations must be satisfied. With this condition, the total derivative equation can be rearranged, as in Equation 17.

$$\underbrace{\frac{d\mathcal{R}}{d\mathbf{x}}}_{n_{\mathcal{R}} \times n_x} = \underbrace{\frac{\partial \mathcal{R}}{\partial \mathbf{x}}}_{n_{\mathcal{R}} \times n_x} + \underbrace{\frac{\partial \mathcal{R}}{\partial \mathbf{u}}}_{n_{\mathcal{R}} \times n_u} \underbrace{\frac{d\mathbf{u}}{d\mathbf{x}}}_{n_u \times n_x} = 0 \qquad \Rightarrow \qquad \frac{d\mathbf{u}}{d\mathbf{x}} = -\left[\frac{\partial \mathcal{R}}{\partial \mathbf{u}}\right]^{-1} \frac{\partial \mathcal{R}}{\partial \mathbf{x}} \tag{17}$$

This result for $d\mathbf{u}/d\mathbf{x}$ can be substituted into Equation 16, to yield

$$\frac{df}{d\mathbf{x}} = \frac{\partial f}{\partial \mathbf{x}} - \overbrace{\underbrace{\frac{\partial f}{\partial \mathbf{u}} \left[\frac{\partial \mathcal{R}}{\partial \mathbf{u}}\right]^{-1}}_{\psi^T} \frac{\partial \mathcal{R}}{\partial \mathbf{x}}}^{\phi} \tag{18}$$

This total derivative equation can be solved in two forms, using either the direct method or the adjoint method. The direct method involves solving a linear system for the quantity ϕ that is equivalent to: $\phi = d\mathbf{u}/d\mathbf{x}$. Instead, the adjoint method involves solving a linear system for the quantity ψ [23]. These linear systems can be written as in equation 19.

$$\underbrace{\frac{\partial \mathcal{R}}{\partial \mathbf{u}}}_{n_u \times n_u} \underbrace{\phi}_{n_u \times n_x} = \underbrace{\frac{\partial \mathcal{R}}{\partial \mathbf{x}}}_{n_u \times n_x} : \text{Direct Method} \qquad \underbrace{\left[\frac{\partial \mathcal{R}}{\partial \mathbf{u}}\right]^T}_{n_u \times n_u} \underbrace{\psi}_{n_u \times 1} = \underbrace{\left[\frac{\partial f}{\partial \mathbf{u}}\right]^T}_{n_u \times 1} : \text{Adjoint Method} \tag{19}$$

The cost of the direct method is dependent on the number of design variables, n_x. In contrast, the cost of the adjoint method is dependent on the number of functions of interest, n_f. In this way, the direct and adjoint methods are notionally similar to forward- and reverse-mode AD, respectively, and can be implemented by using AD on the necessary source code components. The choice of which method to implement is dependent on the number of design variables and functions of interest in the system; when there are fewer design variables than functions of interest, the direct method is favorable, while when there are fewer functions of interest than design variables, the adjoint method is favorable.

These derivative computation techniques can be applied to the coupled aerodynamic-aeroacoustic optimization problem, where there is a single iterative solver in the HBEM component. This solver comprises the solution residual: $\mathcal{R}(\mathbf{x}, \mathbf{u}(\mathbf{x}))$, where the state variable, $\mathbf{u}$, is the scalar thrust magnitude of each simulated rotor at each time-step in the analysis. Consequently, there is one scalar residual value, per rotor, per time-step, and all residuals are independent of each other given the quasi-steady formulation of HBEM. The sparsity in the residual matrix can be utilized to make implicit derivative computation efficient and straightforward to implement.

The required matrices for implicit derivative computation are shown schematically in Figure 4. These matrices represent an associated functional of interest, f, computed for each rotor and each time-step. Given that the HBEM analysis is time-accurate, the functional of interest may be a vector as opposed to a single scalar value. The colored squares in the matrices in Figure 4 represent elements that may be non-zero, meaning that the partial derivative matrix of $\partial f/\partial \mathbf{x}$ may be dense. Since this analysis is quasi-steady, there will be a single quantity of interest per time-step, per rotor. This means that the matrix dimensions are $(n_{\text{time}}n_{\text{rotor}} \times n_x)$. The partial derivative matrix of the functional with respect to the state variables, $\partial f/\partial \mathbf{u}$, is strictly diagonal, as shown in Figure 4, with non-zero entries only on the matrix diagonal. While the matrix is large, with the same number of functional values as state variables $(n_{\text{time}}n_{\text{rotor}} \times n_{\text{time}}n_{\text{rotor}})$, the sparsity can be utilized to compute both the direct or adjoint methods efficiently.

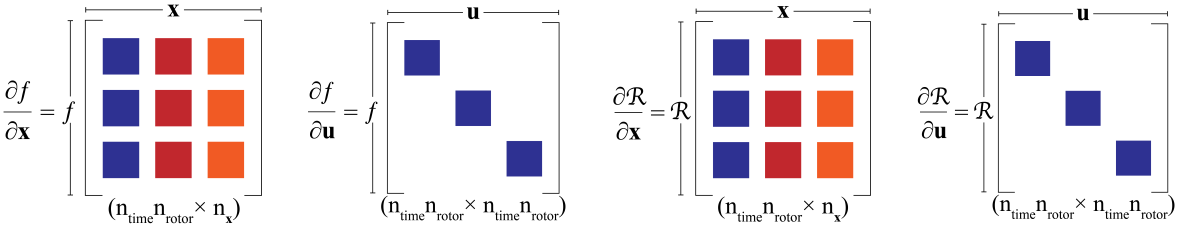

Figure 4: Structure of the matrices required for derivative computation. Squares signify possible non-zero elements with each color requiring a single forward pass of the derivative computation routine.

As with the partial derivatives of the functional with respect to design and state variables, the partial derivatives of the residual with respect to design and state variables must be computed. The partial derivatives of the residual with respect to design variables, $\partial \mathcal{R}/\partial \mathbf{x}$, can be computed efficiently by using a differentiated version of the residual routine used by the iterative solver. The resulting matrix is of size $(n_{\text{time}}n_{\text{rotor}} \times n_x)$, and may be a dense matrix. This result is shown schematically in Figure 4. Instead, the partial derivative matrix of the residual with respect to the state variables, $\partial \mathcal{R}/\partial \mathbf{u}$, can be computed efficiently with a differentiated version of the residual routine used by the iterative solver, but now with derivatives with respect to state variables. As shown schematically in Figure 4, the matrix is strictly diagonal, with non-zero entries only possible on the matrix diagonal. This is because for a single residual found on the desired rotor (i) at the desired time-step (j), $\mathcal{R}_{i,j}$, there exists a single state value $u_{i,j}$ corresponding to the desired rotor and time-step. This matrix is large, of size $(n_{\text{time}}n_{\text{rotor}} \times n_{\text{time}}n_{\text{rotor}})$, but it can be computed in a single forward pass by using derivative coloring. Computing derivatives for the HBEM quasi-steady formulation is particularly efficient, given the derivative matrices' inherent sparsity.

Unifying the aerodynamic and aeroacoustic analysis tools is carried out using OpenMDAO, an open-source multidisciplinary design optimization framework designed to handled coupled systems [21]. The N2 diagram, showing the model structure, coupling, and data passage for the optimization problem within OpenMDAO, is shown in Figure 5. This framework helps handle derivative computation and optimization tasks in a standardized way, implementing required solver routines. The OpenMDAO methodology utilizes the modular analysis and unified derivatives (MAUD) architecture that enables computing derivatives on coupled explicit and implicit analysis components [38, 39]. This formulation generalizes all analysis components as implicit components that must satisfy constraints added within the model. All of the variables in the analysis are transformed into model inputs and outputs, helping to transform the analysis into a monolithic nonlinear system. The unified derivatives equation (UDE) can be applied to the constructed nonlinear system for computing derivatives in optimization [38, 39].

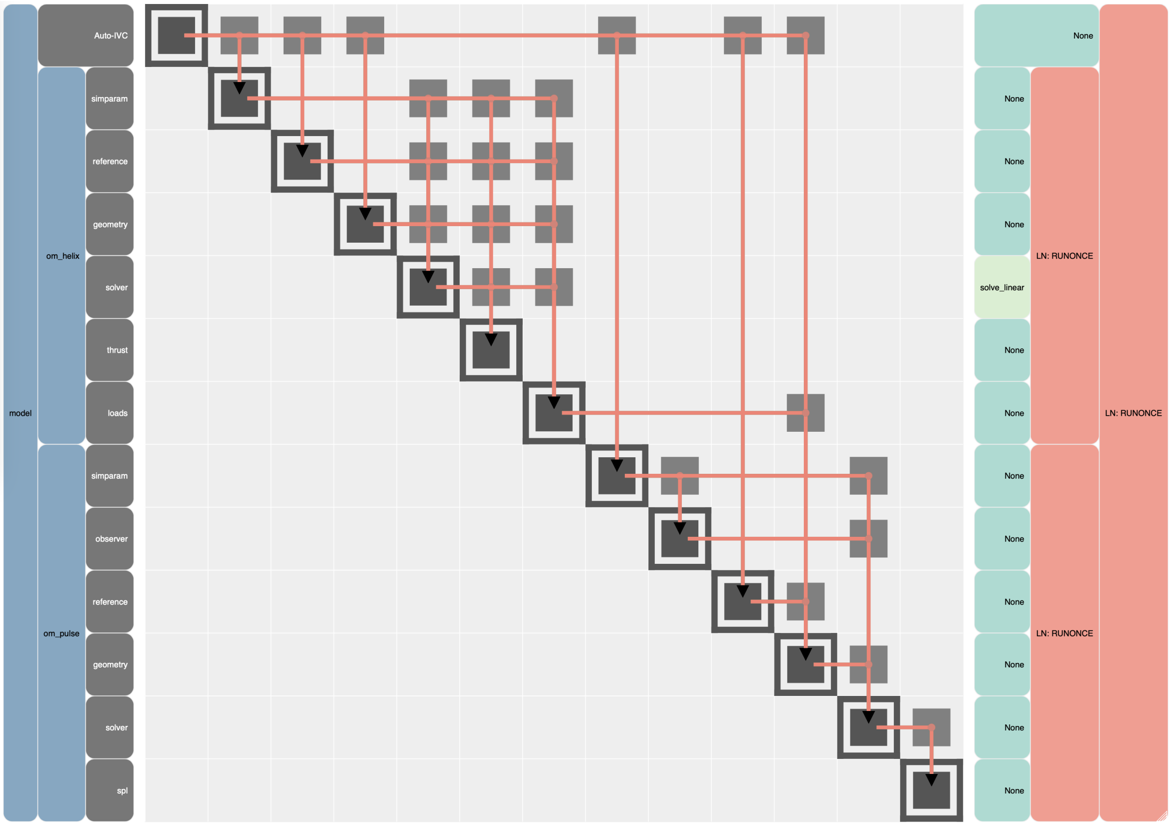

Figure 5: OpenMDAO N2 diagram showing the analysis coupling and flow of data between the models. Diagonal elements represent computational blocks, while off-diagonal elements and red arrows represent component coupling. This model is upper diagonal, meaning that all elements can be computed with a single forward pass.

The N2 diagram, Figure 5, contains diagonal elements that represent computational blocks, while off-diagonal elements and red arrows denote component coupling and flow of data. Given that the iterative solver in the HBEM component is not exposed to OpenMDAO, the model implementation is upper triangular, signifying that a single pass of the OpenMDAO model is required to compute all component values. To compute derivatives, the OpenMDAO model can be configured in forward-mode, traversing it from left to right, or in reverse-mode, traversing it from right to left, depending on which method is more efficient for the particular optimization problem. Each analysis block, wrapped in Python for OpenMDAO, is written in Fortran with the source code necessary for derivative computation differentiated using Tapenade [40] in forward-mode. These analysis components include Python interfaces, using Numpy [41], f2py [42], and f90wrap [43]. The coupled aeroacoustic optimization problem with quasi-steady assumptions can be formulated efficiently to utilize the OpenMDAO framework to perform gradient-based multidisciplinary design optimization.

3 Verification and Validation

3.1 Aerodynamic Analysis Validation

The foundation of BEMT is well established for rotor analysis and has been used and validated extensively. However, many different formulations of the theory exist that lend themselves to other applications. Some methodologies can capture different rotor wake states, while others assume that the rotor is always producing thrust. The HBEM model used in this paper assumes that there exists a well-established slipstream across the rotor that is producing thrust. This formulation has been validated against experimental data obtained from wind tunnel measurements [10]. The validation studies were repeated using HELIX to ensure that the modified implementation for gradient-based optimization is consistent with the original HBEM theory and accurate to experimental data.

Wind tunnel experiments were carried out using an APC MR8x45 small unmanned aerial vehicle rotor[1]. A single rotor was connected to a three-force transducer mounted on a force balance in a wind tunnel. The forces on the rotor were measured for a variety of inlet flow directions and flow velocities. The inlet flow directions range from 0° (axial flow) to 90° (edgewise flow), with measurements carried out at freestream velocities of $V_\infty = 5,\ 10,\ 15$ m/s. The model was validated by comparing various measurements with experimental data, including thrust vs. advance ratio, thrust vs. climb ratio, and thrust vs. angular velocity. To validate HELIX, the thrust vs. angular velocity cases were rerun and compared with experimental data.

The wind tunnel validation results obtained using HELIX are shown in Figure 6, where Figures 6a, 6b, and 6c correspond to the 5, 10, and 15 m/s cases, respectively. Experimental data taken in ten-degree increments is shown as dots, while HELIX results are shown as curved lines. The results for freestream velocity of $V_\infty = 5$ m/s show qualitative agreement between experimental data and computational results, with the HELIX analysis matching experimental results particularly well in edgewise inflow conditions. Additionally, the HELIX results appear to match the experimental trend, with thrust increasing exponentially. The results for freestream velocity of $V_\infty = 10$ m/s again show qualitative agreement in the trend, with better accuracy for edgewise inflow conditions and more significant deviation for axial flight. Similarly, the results for a freestream velocity of $V_\infty = 15$ m/s show the computational results matching the trends of the experimental measurements but under-predicting the thrust generated in axial flight conditions.

These results show that the HBEM formulation within HELIX provides an efficient technique for approximating a rotor's performance and operational trends while

[1] APC Propellers: https://www.apcprop.com/

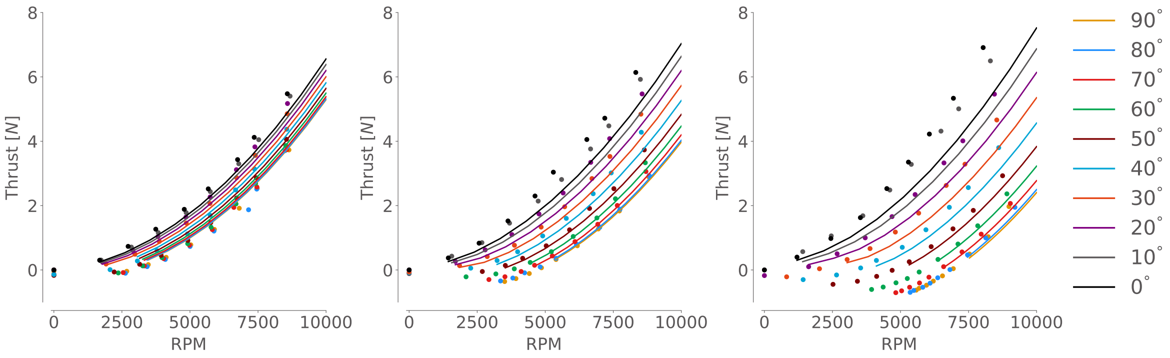

(a) (b) (c)

Figure 6: HBEM theory validation results, HELIX (lines) compared to experimental data (dots). Experimental data reproduced from Davoudi et al. [10] (a) $V_\infty = 5$ m/s (b) $V_\infty = 10$ m/s (c) $V_\infty = 15$ m/s

suffering from accuracy errors, especially when operating in higher freestream flow conditions. This low-fidelity implementation provides a useful starting point for identifying trends in vehicle design and for carrying out gradient-based optimization to understand rotor blade design parameters.

3.2 Aeroacoustic Analysis Validation

The theories and methodologies implemented for aeroacoustic analysis within PULSE have been verified extensively for rotorcraft applications. The formulation used in PULSE, the Farassat Formulation 1A with a compact source-sink assumption for monopole noise, has been implemented in previous rotorcraft studies. The methodology was verified against experimental data from the Higher-Harmonic-Control Aeroacoustic Rotor Test experiments and used for noise prediction of a UH-60 rotor [34]. To ensure that the modified implementation used for gradient-based optimization within PULSE is accurate, the tool was validated against measured data from a parallel blade-vortex-interaction wind tunnel experiment.

Parallel blade-vortex interaction is a phenomenon in which a rotor blade interacts with a vortex filament, momentarily causing a significant pressure perturbation resulting in a spike in noise signal. This phenomenon was studied experimentally using wind tunnel experiments, depicted by the schematic shown in Figure 7a [44]. The experiment consists of an airfoil generating a vortex ahead of a rotor downstream. Microphone measurements were taken throughout the analysis, recording the pressure perturbations caused by the blade-vortex interaction. Given that HBEM, as implemented for his paper, is not able to capture the effects of blade-vortex interaction, a simplified indicial method was used to generate aerodynamic data needed for aeroacoustic analysis [45, 46]. Figure 7b shows a pressure time history over one rotor revolution comparing experimental data with the result simulated using PULSE.

The comparison between experimental measurement and computationally simulated results using PULSE shows that the tool can capture the major noise sources in

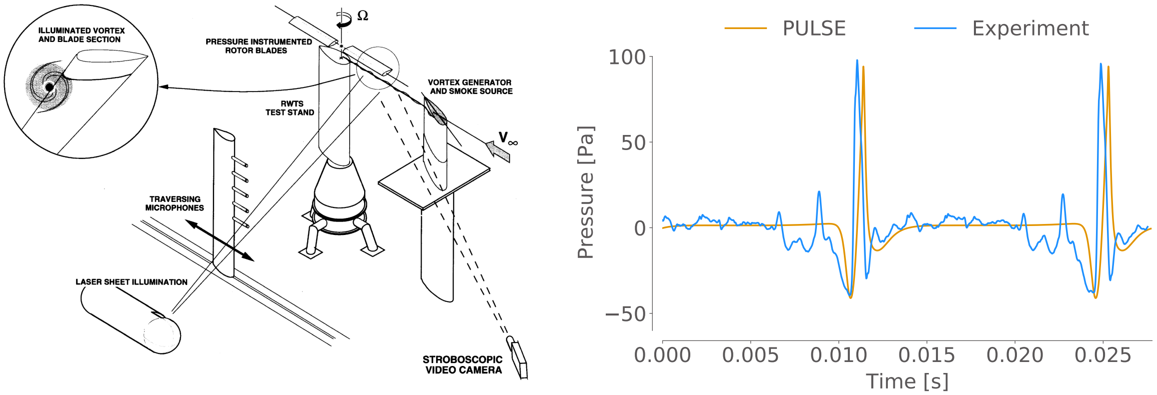

(a)

(b)

Figure 7: Parallel blade-vortex interaction aeroacoustic validation case (a) experimental setup (reproduced from Kitaplioglu et al. [44]) (b) comparison between experimental data [44] and result simulated with PULSE

the pressure time history. While there is a slight offset in phase between the experimental and computational result, PULSE can capture the magnitude and shape of the pressure perturbation caused by the blade-vortex interaction. This result indicates that the aeroacoustic solver within PULSE can correctly resolve pressure perturbation contributions using aerodynamic data, capturing the tonal noise of a rotor in flight.

4 Baseline Analysis

The NASA N+1 single passenger quadrotor with RPM control features four identical rotors, with the rear rotors elevated slightly above the front rotors to avoid interaction in flight. This vehicle was designed and sized using the NASA Design and Analysis of Rotorcraft (NDARC) tool and analyzed using the rotorcraft analysis tool CAMRAD [5]. The quadrotor has been further analyzed with high-fidelity methods to understand its aerodynamic and aeroacoustic performance [47, 48]. While the vehicle design process took into consideration acoustic footprint, the vehicle was not optimized for minimum noise generation. In this work, rotor performance is computed for 360 time-steps over a 0.5-second interval to extract rotor thrust and time-accurate blade loads. This time-history corresponds to approximately five rotor revolutions. The data is transferred to a coupled aeroacoustic analysis tool that interpolates the aerodynamic data in retarded time to 360 timepoints. The sound pressure level is then computed in a uniformly spaced, 10 × 10 grid of observer points located 5 meters below the center of the rotor or vehicle. The simulated rotor performance and sound pressure level are used for gradient-based design optimization.

The data required for blade element analysis includes airfoil properties at each defined blade section. The baseline design sections include four airfoil definitions whose locations along the span of the blade are shown in Figure 8a, which also shows the baseline twist and chord distributions. The rotors are assumed to operate at a collective pitch of 7.767°, applied in addition to the blade twist. Airfoil properties at each defined section were computed using pyXLIGHT, based on the airfoil analysis tool XFOIL with a viscous formulation [49]. The C_l vs. α curves are shown in Figure 8b. Operating conditions for each section, namely Reynolds number and Mach number, were computed using the baseline hover state variables at each corresponding blade location. The airfoil properties at each section were assumed to be fixed at the baseline design values. These results are used to compute the properties necessary for HBEM analysis and interpolated to the number of specified design variables at spanwise locations. The chord and twist values at each specified location serve as design variables during optimization and are further interpolated for higher resolution blade elements in the HBEM solver. Three spanwise design variable resolutions are used in the optimization cases, corresponding to $n = 5$, $n = 10$, and $n = 15$ equally-spaced spanwise sections.

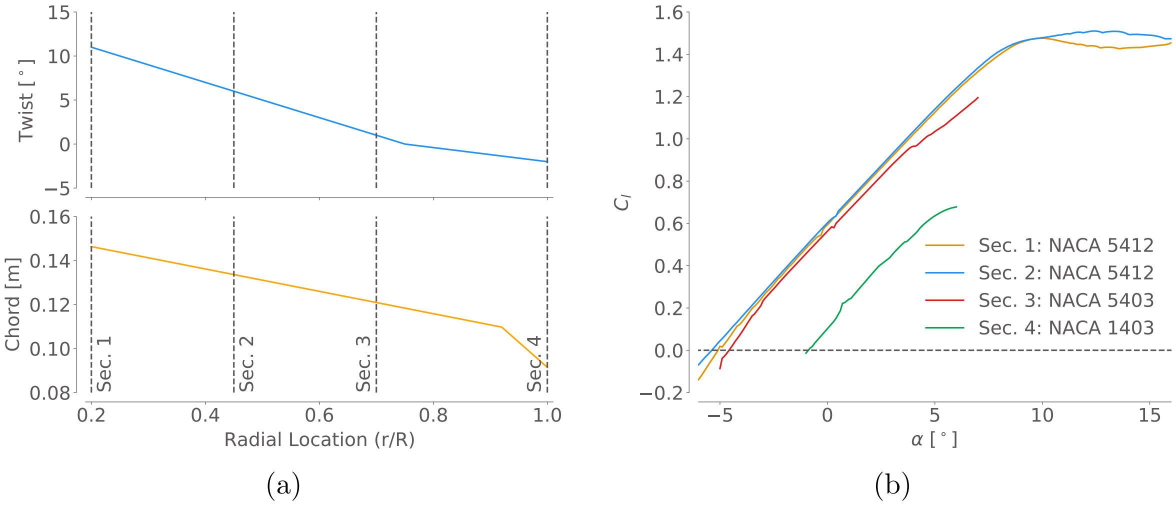

Figure 8: Baseline blade design data for the NASA N+1 quadrotor vehicle (a) twist and chord distributions (b) airfoil C_l vs. α curves in hover flight condition

While the noise footprint of a vehicle is dependent on its complete configuration, an isolated rotor analysis can provide insight into the noise generated by vehicle operation, mainly from loading and thickness noise sources. Figure 9 shows an analysis of an isolated rotor from the N+1 quadrotor, where Figures 9a and 9b show the blade loading and noise footprint, respectively. As the rotor is in hovering flight, both the blade loading and noise footprint are axisymmetric. The blade load distribution shows low loading at the blade's root, increasing towards the blade's center and decreasing at the tip. Given that the HBEM model does not model hub or tip losses, the blade loading is likely higher than the actual performance, especially at the blade extremities. The maximum sound pressure level and total simulated thrust for the $n = 5$, $n = 10$, and $n = 15$ analyses are shown in Tables 1 and 2 for the isolated rotor and quadrotor configurations, respectively. As a comparison, the rotor design thrust is $T_z = 1429.175345$ N [4].

The resulting noise footprint shows a significant decrease in noise directly below

Table 1: Isolated rotor baseline analysis results

n	Maximum SPL [dB]	Thrust [N]
5	71.791254	1425.704352
10	71.954660	1440.569717
15	71.951303	1440.298172

Table 2: Quadrotor baseline analysis results

n	Maximum SPL [dB]	Thrust [N]
5	80.306946	1423.750473
10	80.468196	1438.595466
15	80.464555	1438.324294

the rotor, where pressure perturbations are nearly constant, but an increase in noise radially from the rotor before it decreases further away from the rotor center. This noise analysis considers loading and thickness noise sources but does not capture wake interaction, airfoil self-noise, or high-speed impulsive noise.

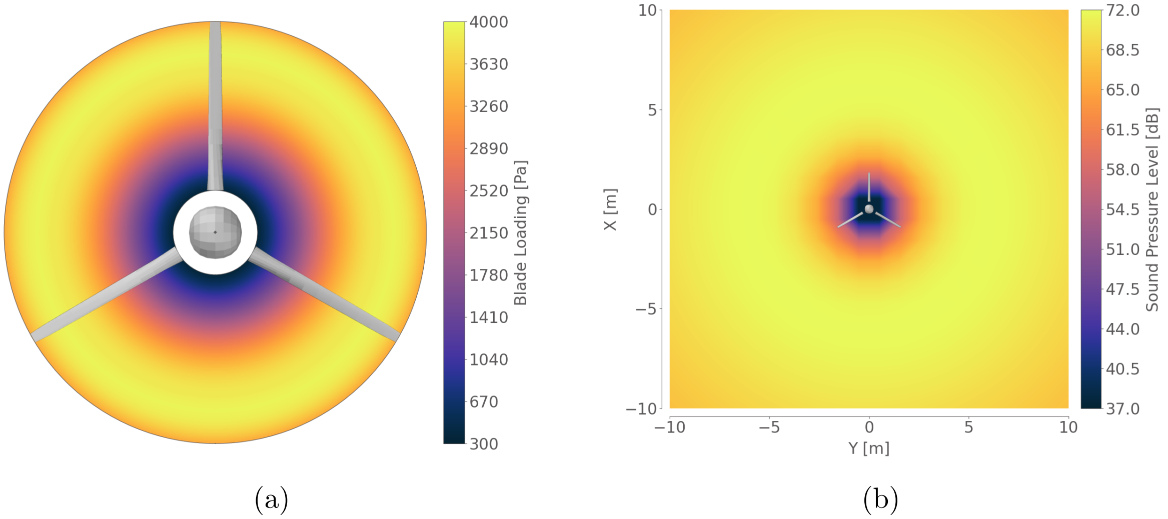

(a)

(b)

Figure 9: NASA N+1 quadrotor isolated rotor base analysis in hover flight condition (a) blade loading (b) sound pressure level five meters below rotor

The complete vehicle analysis is shown in Figure 10, which includes blade loading and noise footprint results in Figures 10a and 10b, respectively. The HBEM model analyzes each rotor individually and does not include a rotor wake, meaning that there is no interaction between the rotors or with the airframe. These simplifications result in axisymmetric blade loading as in the isolated rotor cases. As with the isolated rotor case, the blade loads near the hub and tip of the blades likely overestimate the actual values. However they align closely with the expected vehicle design thrust. Aeroacoustic analysis of the quadrotor shows a patterned footprint, with areas in which pressure perturbations constructively or destructively interact, increasing or decreasing the computed sound pressure level. The noise footprint shows slightly higher noise generation in front of the vehicle because the front rotors are located below the tail rotors, nearer to the observer plane.

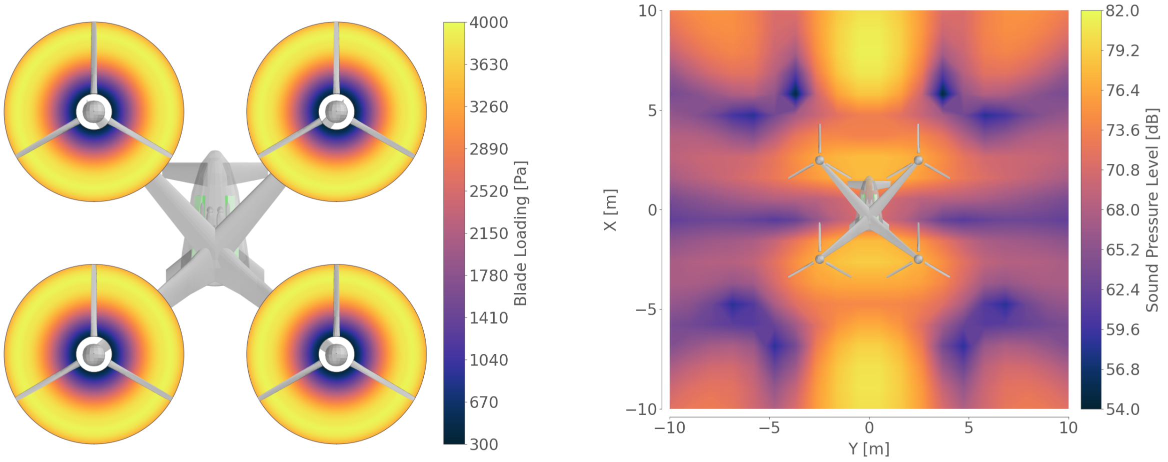

(a)

(b)

Figure 10: NASA N+1 quadrotor vehicle base analysis in hover flight condition (a) blade loading (b) sound pressure level five meters below vehicle

While the HBEM model requires several simplifying assumptions and does not consider rotor or vehicle interaction, it captures baseline trends and vehicle design thrust in hover flight conditions. Similarly, the FWH model with Farassat Formulation 1A and a compact monopole noise model does not account for all sources of noise, including unresolved aerodynamic noise, broadband noise, and high-speed impulsive noise; however, it provides a starting point for understanding the vehicle noise signature and required design choices needed to minimize it.

5 Optimization

The NASA N+1 quadrotor is analyzed using gradient-based optimization to understand how the vehicle design must be modified to better accomplish specific requirements. In this work, gradient-based optimization is used to minimize the peak noise recorded at observer points below an isolated rotor and the quadrotor vehicle while in hover flight conditions. This is done by coupling the HBEM model with aeroacoustic analysis based on the FWH model, Farassat Formulation 1A, and a compact monopole noise source assumption. This coupling is carried out using the optimization software package OpenMDAO that handles data transfer and efficiently computes implicit derivatives. Given the lower implementation cost as compared to the adjoint method with reverse-mode AD, only the direct method and forward-mode AD are used for the presented optimization cases, but the adjoint method can be used for further improvements in derivative computation efficiency.

The quantities of interest in the presented optimizations are the peak sound pressure level recorded at the observer points and the rotor thrust. The rotor design variables of interest are the rotor rotation rate as well as blade twist and chord distributions, taken at equally spaced locations along the blade. Peak sound pressure level across all of the observers is a discontinuous function and is challenging for gradient-based optimization to properly handle. To smooth the discontinuities in the design space, the sound pressure level computed at each observer point is combined using Kreisselmeier–Steinhauser (KS) aggregation [50]. This technique aggregates the recorded values and smooths the design space to improve the robustness of gradient-based optimization. The vehicle thrust is computed using the vertical component of the rotors' thrust. Accurate derivatives for the KS aggregated sound pressure level and thrust values are required to ensure proper optimization convergence.

The derivatives of KS aggregated sound pressure level and thrust for the baseline isolated rotor and quadrotor in hover flight with respect to twist, chord, and rotational rate are shown in Tables 3 and 4, respectively. This table shows a comparison between finite difference, complex step, and the direct method with forward-mode algorithmic differentiation. Blade root, mid-span, and tip location values are shown to display the dominant trends found in derivative precision. The complex step is assumed to be the most accurate derivative, given it is accurate to machine precision. Values in red represent digits in the finite difference and direct method results that are not consistent with the complex step results. The finite difference results provide a check that ensures the derivatives are in the correct range given no source code adaptations but often deviate from the higher-accuracy results. Instead, the direct method more closely matches the complex step derivatives, consistently to over ten significant digits. The accurate direct method derivatives show that it is useful for computing derivatives for optimization analyses.

Table 3: Derivative verification for isolated rotor optimization

Derivatives of KS(SPL) with respect to design variables

Design variable	Finite difference	Complex step	Direct method (fwd AD)
$\text{Twist}_{\text{root}}$	+0000.003821760416031	+0000.003821744395005	+0000.003821744395003
$\text{Twist}_{\text{mid}}$	+0000.285098090767860	+0000.285098140110507	+0000.285098140110512
$\text{Twist}_{\text{tip}}$	+0000.668767511844635	+0000.668767591338044	+0000.668767591338058
$\text{Chord}_{\text{root}}$	+0001.335673168301582	+0001.335673427827338	+0001.335673427827482
$\text{Chord}_{\text{mid}}$	+0031.518437996506691	+0031.518515522804442	+0031.518515522805124
$\text{Chord}_{\text{tip}}$	+0040.713596418499947	+0040.713722625238503	+0040.713722625238859
ω	+0000.597630500793457	+0000.597630413860201	+0000.597630413860206

Derivatives of thrust with respect to design variables

Design variable	Finite difference	Complex step	Direct method (fwd AD)
$\text{Twist}_{\text{root}}$	+0005.263133049011230	+0005.263134830714399	+0005.263134830713834
$\text{Twist}_{\text{mid}}$	+0035.692020177841187	+0035.692032567190267	+0035.692032567191532
$\text{Twist}_{\text{tip}}$	+0052.561220407485962	+0052.561224957196998	+0052.561224957200857
$\text{Chord}_{\text{root}}$	+1090.951535940170288	+1090.951835532580162	+1090.951835532620635
$\text{Chord}_{\text{mid}}$	+5593.705662012100220	+5593.712368640884051	+5593.712368641079593
$\text{Chord}_{\text{tip}}$	+3632.118615388870239	+3632.122797770772195	+3632.122797770873149
ω	+0037.572423458099365	+0037.572422531183776	+0037.572422531184806

Accurate and efficient derivative computation, such as with the direct method, allows for robust gradient-based optimization performance. As with both finite differ-

Table 4: Derivative verification for quadrotor optimization

Derivatives of KS(SPL) with respect to design variables

Design variable	Finite difference	Complex step	Direct method (fwd AD)
$\text{Twist}_{\text{root}}$	+0000.003481596708298	+0000.003481596030981	+0000.003481596030978
$\text{Twist}_{\text{mid}}$	+0000.283218741416931	+0000.283218836384645	+0000.283218836384651
$\text{Twist}_{\text{tip}}$	+0000.664974913001060	+0000.664975038942057	+0000.664975038942072
$\text{Chord}_{\text{root}}$	+0001.283645868301392	+0001.283646359405105	+0001.283646359405259
$\text{Chord}_{\text{mid}}$	+0031.346597746014595	+0031.346677254498111	+0031.346677254498850
$\text{Chord}_{\text{tip}}$	+0040.575448200106621	+0040.575573906853130	+0040.575573906853535
ω	+0000.684826999902725	+0000.684827051490085	+0000.684827051490092

Derivatives of thrust with respect to design variables

Design variable	Finite difference	Complex step	Direct method (fwd AD)
$\text{Twist}_{\text{root}}$	+0005.255920171737671	+0005.255921887346907	+0005.255921887346344
$\text{Twist}_{\text{mid}}$	+0035.643105745315552	+0035.643117877018284	+0035.643117877019549
$\text{Twist}_{\text{tip}}$	+0052.489186048507690	+0052.489191625136087	+0052.489191625139973
$\text{Chord}_{\text{root}}$	+1089.456424474716187	+1089.456723957548547	+1089.456723957589702
$\text{Chord}_{\text{mid}}$	+5586.039682865142822	+5586.046380246750232	+5586.046380246946683
$\text{Chord}_{\text{tip}}$	+3627.140921831130981	+3627.145099709305214	+3627.145099709406622
ω	+0037.520931005477905	+0037.520930831918349	+0037.520930831919351

ence and complex step, the direct method scales with the number of design variables, increasing in cost with increasing number of design variables. For the optimization cases in this work, the number of design variables is maintained as $\mathcal{O}(10)$ to ensure reasonable computational cost. Each optimization case was repeated with three design variable resolutions corresponding to $n = 5$, $n = 10$, and $n = 15$ spanwise design variable locations. The number of blade elements and the resolution of the simulations was kept approximately constant across all analyses. Furthermore, to improve optimization robustness, all design variable, constraint function, and objective function values are scaled to be $\mathcal{O}(1)$. All optimizations converged to a tolerance of 10^{-6} using the optimizer Scipy SLSQP [51] wrapped within the package pyOptSparse [52]. The cases ran with OpenMP parallelism using a 6 core (12 thread) 3.6GHz Intel Xeon E5-1650 v4 processor.

5.1 Twist and Angular Velocity Optimization

The optimization problem statement for rotor blade twist and rotation rate optimization is shown in Table 5. This optimization intends to minimize the KS aggregated sound pressure level across all of the observers below the rotor or vehicle with respect to the blade twist distribution and rotational rate. This optimization is intended for hover flight, so the vertical component of lift generated by each rotor is constrained to one-quarter the total weight of the quadrotor vehicle. In total, this optimization consists of one objective function, one constraint function, and 6, 11, or 16 design variables for $n = 5$, $n = 10$, and $n = 15$, respectively.

The optimization results for an isolated rotor in hover flight are shown in Table 6. These results show the objective function converging to a similar value for $n = 10$ and $n = 15$, but converging slightly higher for $n = 5$. This difference is due to the limited

Table 5: Optimization problem statement for rotor blade twist, and rotational rate optimization.

	Function or Variable	Units	Description	Quantity
minimize	KS(SPL)	dB	KS aggregated sound pressure level	1
with respect to	Twist	°	Blade twist distribution	5/10/15
	ω	rad/s	Rotor rotation rate	1
			Total design variables	6/11/16
subject to	$\text{Thrust}_z = 1429.175345$	N	Single rotor thrust required for 1/4 vehicle weight	1
			Total constraints	1

design freedom of the $n = 5$ case, where the individual blade sections are interpolated over greater spans. The optimization cases satisfied the vertical thrust requirement and reduced the noise by approximately 1 dB from the baseline design. The performance of the optimization cases, documented in the table, show that the cost of the cases increased as the design variable resolution increased. Given the optimizations were carried out using the direct method, the cost of computing derivatives scaled with the number of inputs. Additionally, the time required to compute derivatives is much greater than individual calls to the objective function and increases with an increasing number of design variables.

Table 6: Optimization results for isolated rotor twist and rotational rate optimization

n	Obj. Value [dB]	Cons. Value [N]	Obj. Func. Calls	Obj. Func. Time [s]	Deriv. Func. Calls	Deriv. Func. Time [s]	Total Time [s]
5	71.142407	1429.175181	29	258.2924	25	1897.0652	2155.3936
10	70.955733	1429.175344	48	639.3215	47	5997.5666	6636.9332
15	70.957564	1429.174310	51	435.1606	50	9332.5599	9767.7854

The optimized twist distributions along the span of the blade for the three design variable resolutions are shown in Figure 11. All three cases appear to converge to the same blade design, with rotational rates of 71.924574, 71.320241, and 71.324824 rad/s for $n = 5$, $n = 10$, and $n = 15$, respectively. Compared to the baseline design, the optimized rotor operates at a lower rotational rate but with an increased twist. The twist of the blade is high at the root before decreasing substantially in the outboard direction. The decrease in twist diminishes with increasing radial distance from the root, meaning that the twist flattens and appears consistent towards the blade's tip. Increased twist, particularly near the blade's root, yields a modified blade load distribution and consequently a modified noise footprint.

Figure 12 shows simulation results for the $n = 15$ twist optimized blade, with Figure 12a showing blade loading distribution and Figure 12b showing the acoustic footprint. The optimized design shows an increase in peak disk loading, compensating for the decreased rotor rotation rate, with loading moved outboard towards the tip of the blades. While tip or hub loses are not properly captured in the analysis, this result suggests that the noise footprint can be decreased by increasing blade loading and decreasing rotor rotation rate. The resulting noise footprint is axisymmetric,

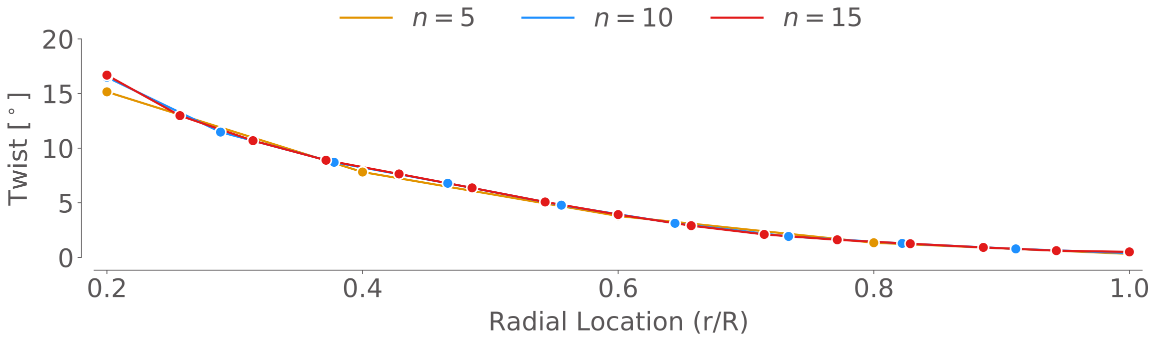

Figure 11: Isolated rotor twist and rotation rate optimization, twist distribution

matching the expected result as the analysis itself is axisymmetric. The noise footprint qualitatively matches the baseline design footprint, however, with decreased sound pressure levels.

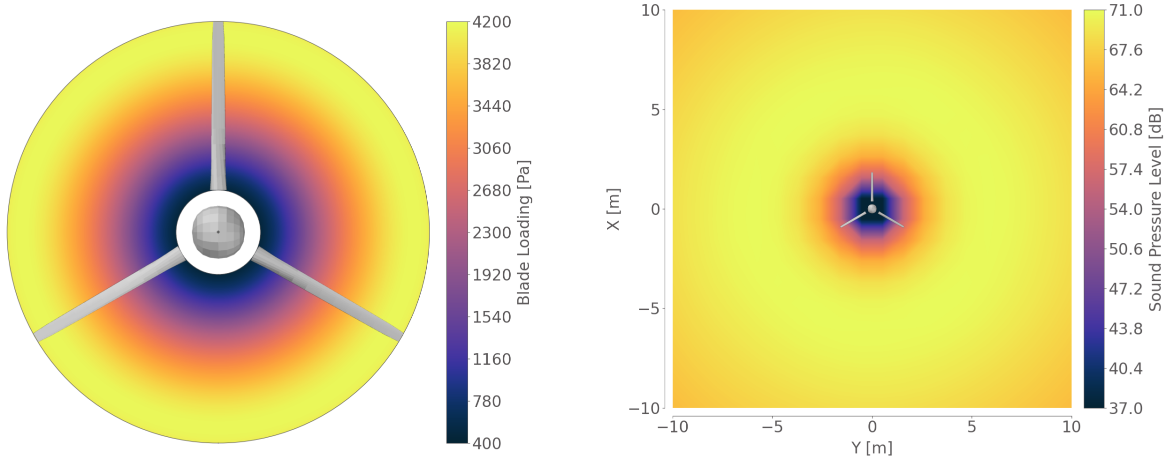

(a)

(b)

Figure 12: NASA N+1 quadrotor isolated rotor twist and rotation rate $n = 15$ optimization result in hover flight condition (a) blade loading (b) sound pressure level five meters below rotor

The optimization results for the quadrotor in hover flight are shown in Table 7. The optimized objective function value converged to approximately the same result for $n = 5$, $n = 10$, and $n = 15$, converging slightly higher for the $n = 5$ case. As with the isolated rotor cases, this deviation in the result is likely due to the limited design freedom in the $n = 5$ case. The cases satisfied the vertical thrust requirement and reduced the noise by approximately 1 dB, similar to the isolated rotor results. This optimization has a higher cost than the isolated rotor case, as the aerodynamic and aeroacoustic simulations require more computations; however, the size of the optimization problem is the same as the isolated rotor. The required time for objective and derivative function evaluations is greater than that of the isolated rotor case; however the number of iterations is not.

Table 7: Optimization results for quadrotor twist and rotational rate optimization

n	Obj. Value [dB]	Cons. Value [N]	Obj. Func. Calls	Obj. Func. Time [s]	Deriv. Func. Calls	Deriv. Func. Time [s]	Total Time [s]
5	79.822446	1429.174046	24	776.2033	24	7017.0377	7793.2731
10	79.392263	1429.174415	42	1329.6736	41	20400.6397	21730.3668
15	79.393482	1429.175071	56	1819.9286	53	386000.0685	40420.0954

Figure 13 shows the optimized twist distributions along the blade for the three design resolutions, corresponding to optimized rotor rotation rates of 73.848519, 71.369529, and 71.375552 rad/s for $n = 5$, $n = 10$, and $n = 15$, respectively. As with the isolated rotor cases, all three resolutions appear to converge to a similar twist distribution. The higher resolution cases more closely match in distribution and rotation rate. The twist along the blade is increased, with the root featuring a substantially increased twist, decreasing towards the tip. Similar to the isolated rotor case, this distribution increases the loading on the blade, particularly near the tip, to compensate for the decreased rotation rate.

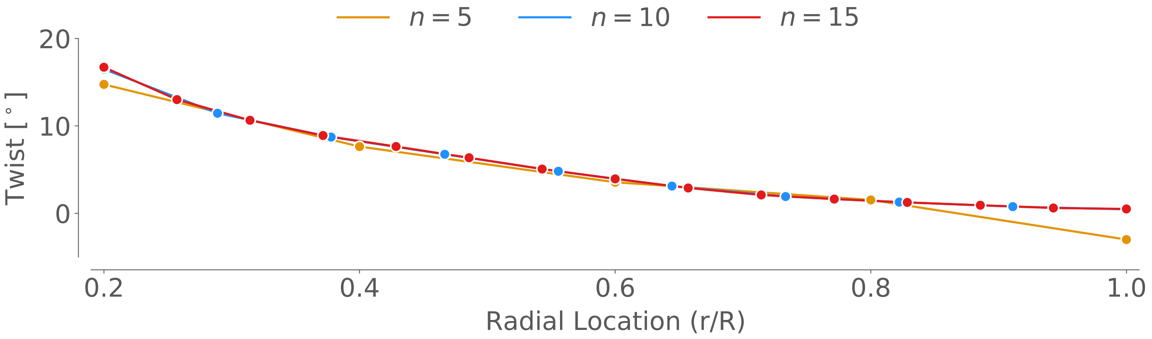

Figure 13: Quadrotor twist and rotation rate optimization, twist distribution

Figure 14 shows simulation results of the $n = 15$ twist optimized quadrotor, where Figure 14a shows the blade loading over one rotor revolution. Similar to the isolated rotor case, the blade loading is increased, particularly near the blade's tip. This increase in loading near the tip is likely over-estimated as both hub and tip losses are not accounted for. However, this suggests that increased loading can be used to decrease rotor rotation rate and consequently noise generation. The optimized noise footprint is shown in Figure 14b, where the noise pattern appears to qualitatively match the footprint of the baseline design, with only a small decrease in overall magnitude attributed to the optimized twist distribution and rotation rate for the rotors.

For both the isolated rotor and quadrotor designs, the optimizations decreased the peak sound pressure level below the vehicle by approximately 1 dB. This decrease was accomplished by increasing the blade twist and consequently increasing blade loading while decreasing the rotor rotation rate. However, this result yields only a small improvement in noise generation, suggesting that other design variables are relevant for decreasing rotor noise.

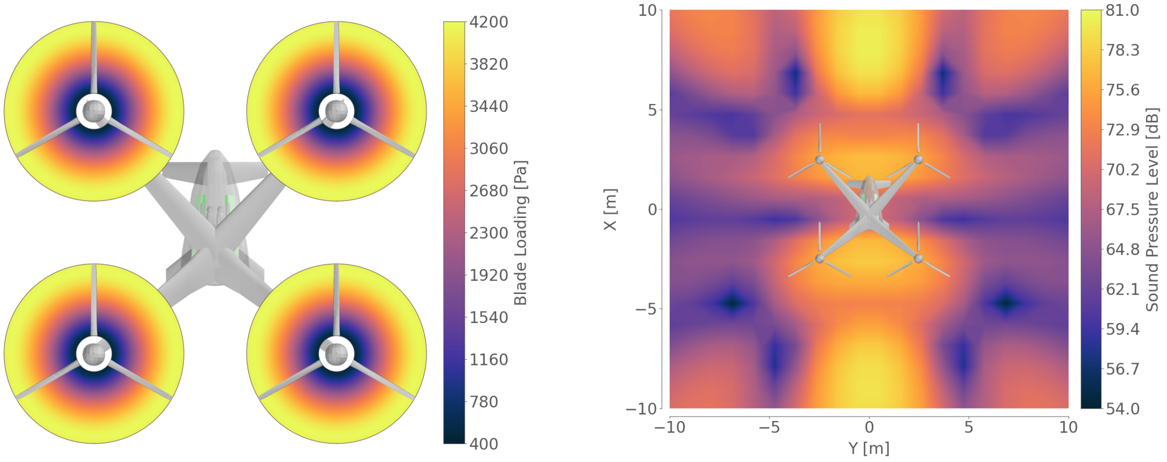

(a)

(b)

Figure 14: NASA N+1 quadrotor twist, and rotation rate $n = 15$ optimization result in hover flight condition (a) blade loading (b) sound pressure level five meters below rotor

5.2 Twist, Chord, and Angular Velocity Optimization

An optimization problem statement for a twist, chord, and rotation rate optimization is shown in Table 8. The objective of this optimization is to minimize the KS aggregated sound pressure level across all of the observers below the rotor or vehicle with respect to the blade twist distribution, chord distribution, and rotational rate. The rotor or vehicle's flight condition is hover, so each rotor is constrained to provide one-quarter of the total weight of the vehicle in the vertical direction. To avoid unphysical results, given that structural constraints and important considerations such as rotor efficiency are not included in the optimization cases, the chord design variables are bounded within a range of $0 - 0.2$ m. In total, this optimization consists of one objective function, one constraint function, and 11, 21, and 31 design variables for $n = 5$, $n = 10$, and $n = 15$, respectively.

Table 8: Optimization problem statement for rotor blade twist, chord, and rotational rate optimization.

	Function or Variable	Units	Description	Quantity
minimize	KS(SPL)	dB	KS aggregated sound pressure level	1
with respect to	Twist	°	Blade twist distribution	5/10/15
	Chord	m	Blade chord distribution	5/10/15
	ω	rad/s	Rotor rotation rate	1
			Total design variables	11/21/31
subject to	$\text{Thrust}_z = 1429.175345$	N	Single rotor thrust required for 1/4 vehicle weight	1
			Total constraints	1

The optimization results for an isolated rotor in hover flight are shown in Table 9. The results show the objective function converging to a similar value across the three cases, with minor discrepancy. The optimization satisfies the vertical thrust requirement and reduced the maximum noise generated by approximately 6 dB. The table also shows the performance of the optimization, where the cost increased with an increasing number of design variables. Given the additional chord design variables, the case is more computationally expensive than the twist and rotation rate isolated rotor optimization.

Table 9: Optimization results for isolated rotor twist, chord, and rotational rate optimization

n	Obj. Value	Cons. Value	Obj. Func.	Obj. Func.	Deriv. Func.	Deriv. Func.	Total Time
	[dB]	[N]	Calls	Time [s]	Calls	Time [s]	[s]
5	65.674737	1429.174272	51	436.4621	48	6320.3873	6756.9149
10	65.608959	1429.174139	127	1704.1003	91	21640.0461	23344.2564
15	65.484084	1429.175417	195	1744.8453	128	46702.8504	48447.9238

Figure 15 shows the optimized twist and chord distributions for the three design variable resolutions that correspond to optimized rotor rotation rates of 66.662961, 64.09378158 , and 62.90260313 rad/s for $n = 5$, $n = 10$, and $n = 15$, respectively. The twist distribution on the blade is increased near the root of the blade and decreases in the outboard direction. The change in twist decreases over the span of the blade before increasing near the tip. The three design variable resolutions deviate in result for the tip section of the blade but follow a similar trend of decreasing twist. The chord distribution shows the value is uniformly set to the maximum allowed value of 0.2 m, meaning that an increased area can be beneficial for decreased rotor noise generation. The increased area due to a longer chord length allows for a lower rotor rotation rate and lower tip loading, decreasing the pressure perturbation that is generated by the high-speed rotor tip.

Figure 16 shows the blade loading and aeroacoustic footprint of the $n = 15$ optimized isolated rotor. The blade loading, shown in Figure 16a, is lower and more uniform across the entire blade than the baseline case, largely due to its increased area. The blade's tip has a dramatic decrease in loading that becomes negative. This negative loading is poorly captured with the HBEM methodology, as root and tip losses are not captured, and the inflow model does not necessarily capture this inflow condition. However, the significant decrease in blade twist and consequent negative blade loading is a useful result that can likely be attributed to the optimizer attempting to remove loading from the tip of the blade, as the increased area of the remainder of the blade is capable of providing the required lift without the tip section. The optimized sound pressure level, shown in Figure 16b, shows the same pattern as the baseline isolated rotor analysis and is axisymmetric. The decreased sound pressure level is due to a decrease in the overall sound pressure level throughout all observer points.

The optimization results for the quadrotor in hover flight are shown in Table 10. The optimized objective function value converged to a similar result for $n = 5$, $n = 10$, and $n = 15$, although with minor deviation. The results satisfy the thrust requirement and decrease the peak noise by approximately 7 dB. The performance of the optimization cases is also shown in the table. While the size of the optimization cases is the same

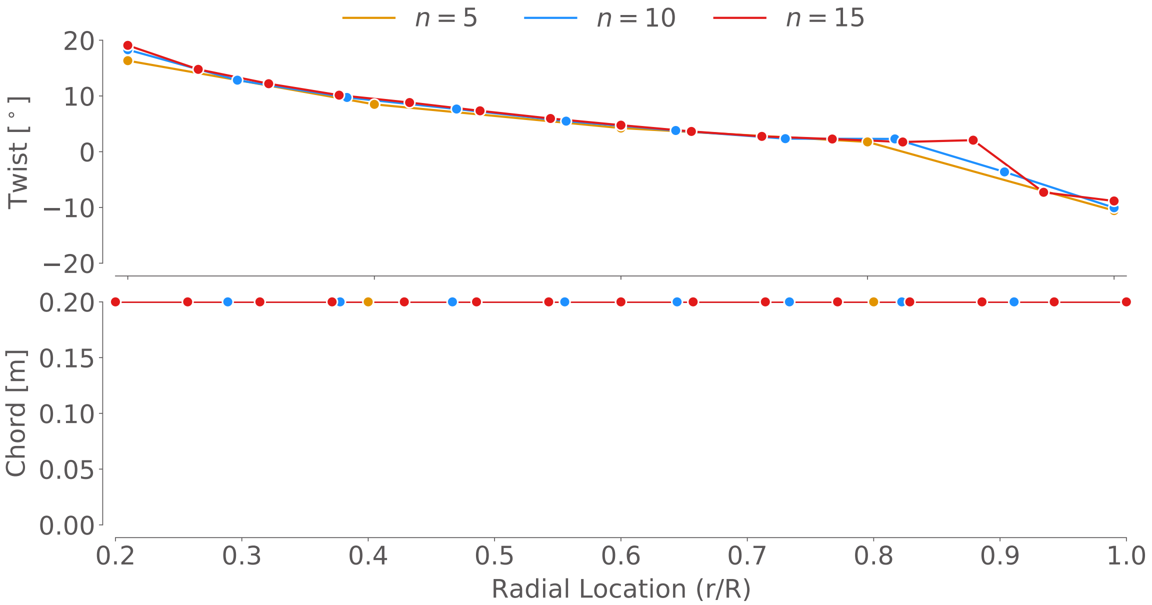

Figure 15: Isolated rotor twist, chord, and rotation rate optimization, twist and chord distributions

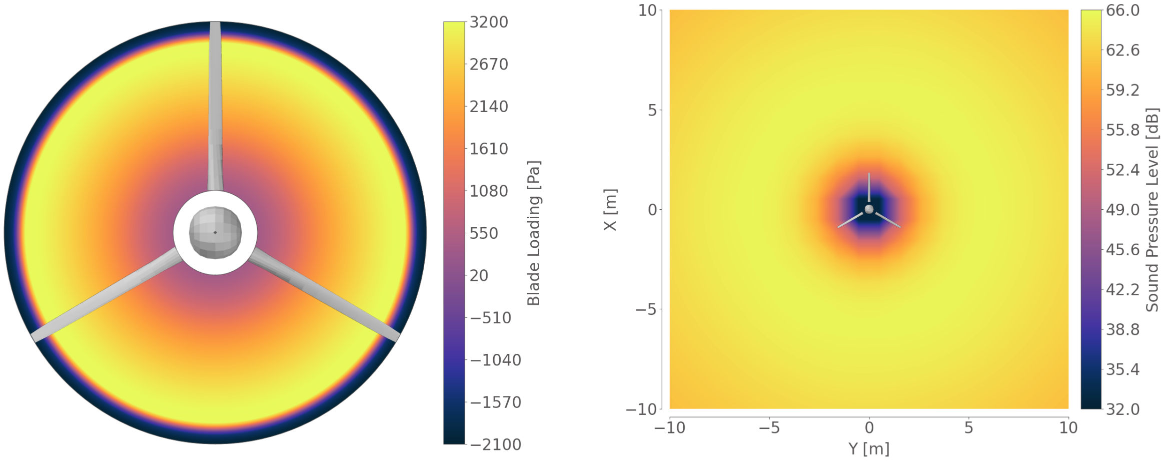

(a) (b)

Figure 16: NASA N+1 quadrotor isolated rotor twist, chord, and rotation rate $n = 15$ optimization result in hover flight condition (a) blade loading (b) sound pressure level five meters below rotor

as the isolated rotor, the cost increases because each analysis is more computationally expensive with additional rotors. Furthermore, the added chord design variables cause the optimization wall time to increase substantially beyond the other optimization cases.

Figure 17 shows the optimized twist and chord distributions for each spanwise variable resolution. These curves correspond to optimized rotor rotation rates of 65.713951, 56.580455, and 61.128316 rad/s for $n = 5$, $n = 10$, and $n = 15$, respectively. These

Table 10: Optimization results for quadrotor twist, chord, and rotational rate optimization

n	Obj. Value [dB]	Cons. Value [N]	Obj. Func. Calls	Obj. Func. Time [s]	Deriv. Func. Calls	Deriv. Func. Time [s]	Total Time [s]
5	74.231399	1429.174222	47	1521.3968	46	23482.4716	25003.9296
10	73.425789	1429.174343	71	2325.4775	68	62704.3419	65029.9127
15	73.856633	1429.174531	114	3688.4223	111	153560.8219	157249.4048

values deviate substantially from each other, signifying the optimizer has found multiple designs that converge to the required optimization tolerance. As with the isolated rotor case, the twist increases at the root of the blade, and decreases towards the tip. Both $n = 5$ and $n = 15$ increase the tip area to the maximum allowed value while significantly decreasing the twist on the tip. Instead, the $n = 10$ case does not increase the tip chord length and does not substantially change the twist at the tip of the blade. The chord distribution for the remainder of the blade shows that the optimization arrived at a design that is as large as permitted, with each chord section set to the maximum allowed value of 0.2 m. As with the isolated rotor case, the increased area allows for a lower rotor rotation rate and decreased tip loading, decreasing the noise generated by the rotor, especially from the tip of the blade. The deviation in result may be explained as the optimizer approaching the optimum with a different approach in each case. A stricter tolerance may help to converge to the same result for each case.

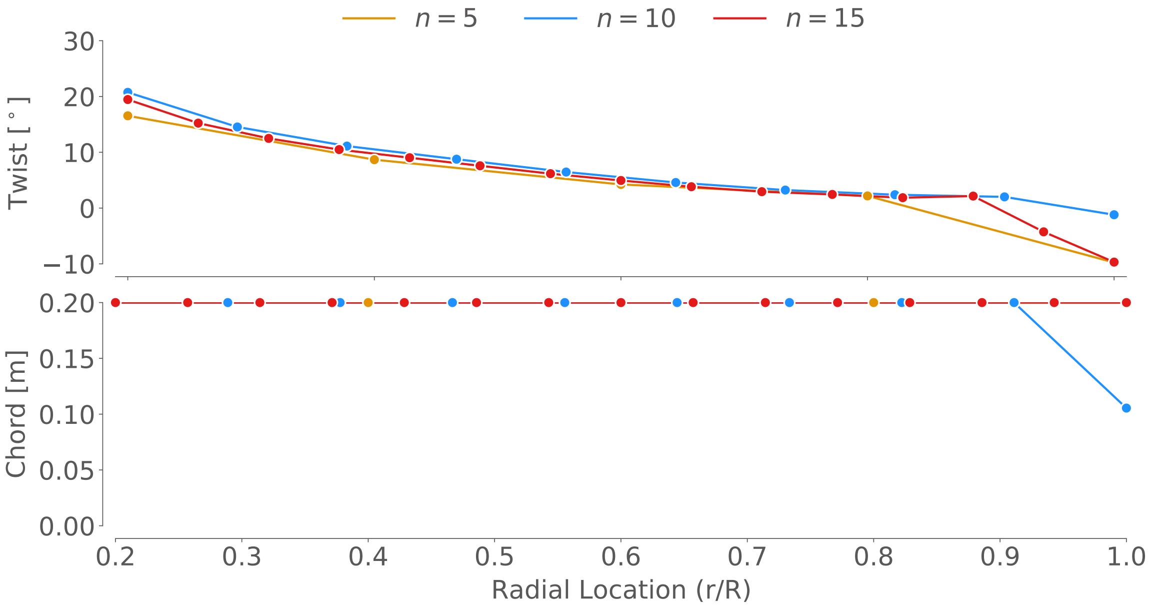

Figure 17: Quadrotor twist, chord, and rotation rate optimization, twist and chord distributions

Figure 18 shows the $n = 15$ optimized rotor design analyzed for blade loads and aeroacoustic footprint, in Figures 18a and 18b, respectively. As in the isolated rotor case, the blade loading of each rotor on the quadrotor is uniformly decreased across the blade, with a sharp decrease at the tip.

The negative loading at the tip is likely because the remainder of the blade can generate the required thrust, with the optimizer attempting to unload the tip to decrease high-speed pressure perturbations. The negative loading is not well captured without accounting for root and tip losses, and with the fixed linear inflow model. However, it provides insight into design improvements that can be made to decrease the noise the rotor generates. The vehicle noise footprint shows that the optimized design generates a similar pattern to that of the baseline design, albeit decreased across all observer points. This is likely due to the increased blade area that allows for decreased rotor rotation rate without requiring an increase in the loading on each blade.

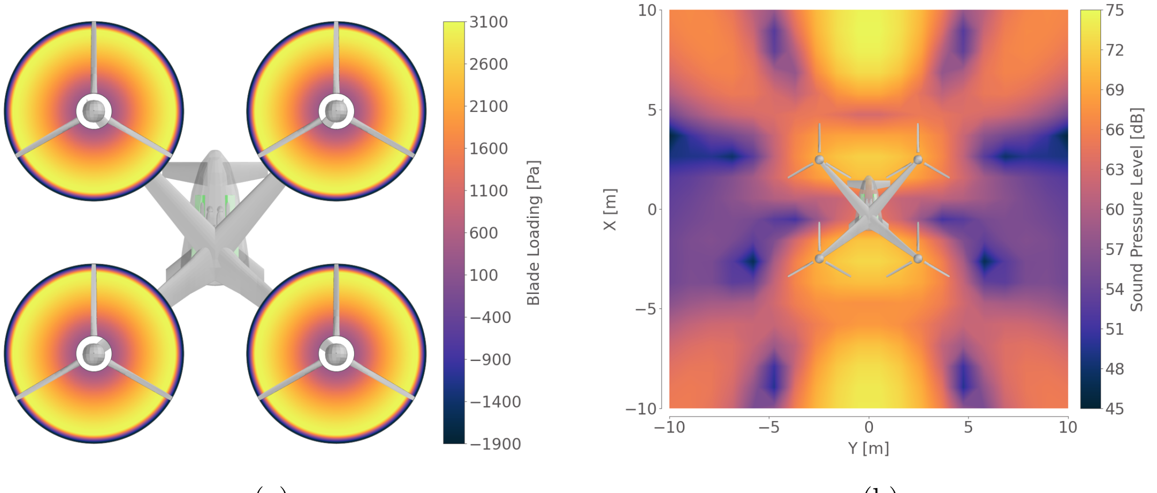

(a)

(b)

Figure 18: NASA N+1 quadrotor twist, chord, and rotation rate optimization $n = 15$ result in hover flight condition (a) blade loading (b) sound pressure level five meters below rotor

Both the isolated rotor and quadrotor designs were optimized to decrease the peak sound pressure level recorded on the defined grid of observers, yielding an improvement of approximately $6 - 7$ dB. This decrease was accomplished by increasing the chord distribution to the maximum allowed value and increasing the blade twist near the root and across the blade span, with a sharp decrease in loading at the blade tip, along with decreasing the rotational rate of the rotors. The loading at the blade tip is negative, which is not well captured by the HBEM model without root or tip loss models and a fixed inflow model. However, the result provides intuition into the optimizer attempting to remove loading from the blade tip. The lack of flexibility in the optimization and linear interpolation between defined sections likely causes the optimizer to find a result in which some elements generate negative loading.

6 Conclusion and Discussion

The emergence of UAM is driving the rapid development of novel aerial vehicles that are taking shape as complex rotorcraft. These rotorcraft are intended to fly over cities to safely and efficiently transport passengers; however, they must do so without causing great disturbance to the communities they are intended to serve. To ensure quiet vehicles which can operate within noise regulations, UAM vehicle design should consider aeroacoustic performance throughout the vehicle design process. This can be done by developing efficient computational methods that can be used for multidisciplinary analysis and gradient-based design optimization. In this paper, we present a hybrid blade element momentum (HBEM) model coupled with an acoustics analysis tool that considers monopole and dipole noise for gradient-based rotorcraft optimization. Both tools are algorithmically differentiated in forward-mode, and model derivatives are obtained using the direct method implemented through the OpenMDAO framework. We use this coupled model to optimize the rotors on the NASA N+1 quadrotor vehicle, considering twist, chord, and rotation rate design variables for both isolated rotor and quadrotor cases.

The optimization analyses show that the noise generated by an isolated rotor and quadrotor can be decreased by 1 dB by optimizing the blade twist distribution and rotor rotational rate, increasing blade loading while decreasing rotational rate. This decrease in noise does not cause a change in qualitative noise footprint, instead a uniform decrease across the entire observer field. Including the chord design variable within the optimization leads to a greater decrease in the noise of 6–7 dB by increasing the chord at each blade section to redistribute loading while also allowing for a lower rotational rate. These results provide insight into low-noise rotor design with blade twist, chord, and rotational rate design variables. The coupled models can be used with greater design freedom to further understand the aeroacoustic performance of the entire vehicle and the blade designs, leading to decreased noise generation.

The work presented in this paper showcases the coupled models that can be used for efficient and time-accurate gradient-based optimization with aeroacoustic considerations. Continuing work is focused on improving the efficiency of the optimization using the adjoint method with reverse-mode algorithmic differentiation. Furthermore, in its current form, the HBEM model can represent quasi-steady and azimuthally varying inflows, but it does not consider unsteady and impulsive contributions to blade loading. Such corrective models are being added to the HBEM model to improve its accuracy. Finally, the aeroacoustic formulation used in this paper accounts for tonal noise in the form of dipole (loading) and monopole (thickness) noise sources. A broadband noise model can provide additional insight into the total noise a vehicle generates while in operation, helping to minimize its complete noise footprint. Using efficient modeling and gradient-based optimization techniques such as blade element modeling and aeroacoustic analogies helps to provide insight into low-noise vehicle design that can be used throughout a vehicle design process.

Acknowledgments

The authors thank the Hyundai Motor Company for funding this research and are grateful to Mr. Christopher Silva and the Aeromechanics Branch at NASA Ames Research Center for sharing design data for the NASA N+1 Vehicle concepts.

References

[1] Antcliff, K. R., Whiteside, S. K. S., Kohlman, L. W., and Silva, C., "Baseline Assumptions and Future Research Areas for Urban Air Mobility Vehicles," *AIAA Scitech 2019 Forum*, San Diego, California, 2019, pp. 1–18. doi:10.2514/6.2019-0528.

[2] Moore, M. D., "Personal Air Vehicles: A Rural/Regional and Intra-Urban On-Demand Transportation System," *Journal of the American Institute of Aeronautics and Astronautics (AIAA)*, AIAA, Dayton, Ohio, 2003, pp. 1–20.

[3] Moore, M., Goodrich, K., and Patterson, M., "ODM Technical Roadmap Report Out - Transformative Vertical Flight Workshop," Tech. rep., NASA Aeronautics Research Mission Directorate, Hartford, Connecticut, 2016.

[4] Johnson, W., Silva, C., and Solis, E., "Concept Vehicles for VTOL Air Taxi Operations," *Proceedings of the AHS technical conference on Aeromechanics Design for Transformative Vertical Flight*, 2018.

[5] Johnson, W., and Silva, S., "Observations from Exploration of {VTOL} Urban Air Mobility Designs," Presentation, Aeromechanics Branch - NASA Ames Research Center, Jeju Island, Korea, oct 2018.

[6] Silva, C., Johnson, W., Antcliff, K. R., and Patterson, M. D., "VTOL Urban Air Mobility Concept Vehicles for Technology Development," *AIAA Aviation 2018 Forum*, AIAA AVIATION Forum, Atlanta, Georgia, 2018, pp. 1–16.

[7] Brelje, B., and Martins, J. R. R. A., "Electric, Hybrid, and Turboelectric Fixed-Wing Aircraft: A Review of Concepts, Models, and Design Approaches," *Progress in Aerospace Sciences*, Vol. 104, 2019, pp. 1–19. doi:10.1016/j.paerosci.2018.06.004.

[8] Glauert, H., "A General Theory of the Autogyro," Reports and Memoranda 1111, Aeronautical Research Committee, 1926.

[9] Gill, R., and D'Andrea, R., "Propeller thrust and drag in forward flight," *1st Annual IEEE Conference on Control Technology and Applications, CCTA 2017*, 2017, pp. 73–79. doi:10.1109/CCTA.2017.8062443.

[10] Davoudi, B., and Duraisamy, K., "A Hybrid Blade Element Momentum Model for Flight Simulation of Rotary Wing Unmanned Aerial Vehicles," *AIAA Aviation Forum*, Dallas, Texas, 2019, pp. 1–21. doi:10.2514/6.2019-2823.

[11] Ning, A., "A Simple Solution Method for the Blade Element Momentum Equations with Guaranteed Convergence," *Wind Energy*, Vol. 17, No. 9, 2014, pp. 1327–1345. doi:10.1002/we.1636.

[12] Ning, A., "Using blade element momentum methods with gradient-based design optimization," *Structural and Multidisciplinary Optimization*, 2021. doi:10.1007/s00158-021-02883-6.

[13] Ffowcs Williams, J. E., and Hawkings, D. L., "Sound Generation by Turbulence and Surfaces in Arbitrary Motion," Tech. Rep. 1151, Royal Society, 1969.

[14] Brentner, K. S., "Modeling aerodynamically generated sound: Recent advances in rotor noise prediction," *38th Aerospace Sciences Meeting and Exhibit*, Reno, Nevada, 2000, pp. 1–11. doi:10.2514/6.2000-345.

[15] Farassat, F., "Derivation of Formulations 1 and 1A of Farassat," Tech. rep., NASA Center for AeroSpace Information, 2007.

[16] Brentner, K. S., Zolbayar, B.-E., and Jaworski, T. F., "An investigation of noise from electric, low-tip-speed aircraft propellers," *Proceedings of the AHS International Technical Meeting on Aeromechanics Design for Transformative Vertical Flight 2018*, San Francisco, California, 2018, pp. 1–12.

[17] Zawodny, N. S., Boyd, D. D., and Burley, "Acoustic Characterization and Prediction of Representative, Small-Scale Rotary-Wing Unmanned Aircraft System Components," *American Helicopter Society*, West Palm Beach, Fl, 2016, pp. 1–15.

[18] Zawodny, N. S., and Boyd, D. D., "Investigation of rotor-airframe interaction noise associated with small-scale rotary-wing unmanned aircraft systems," *AHS 73rd Annual Forum*, Fort Worth, Texas, 2017, pp. 1–17. doi:10.4050/jahs.65.012007.

[19] Zawodny, N. S., Christian, A., and Cabell, R., "A Summary of NASA Research Exploring the Acoustics of Small Unmanned Aerial Systems," *AHS Specialists Conference on Aeromechanics Design for Transformative Vertical Flight*, San Francisco, California, 2018, pp. 1–11. URL `https://ntrs.nasa.gov/search.jsp?R=20180002208`.

[20] Whiteside, S. K. S., Zawodny, N. S., Fei, X., Pettingill, N. A., Patterson, M. D., and Rothhaar, P. M., "An Exploration of the Performance and Acoustic Characteristics of UAV-Scale Stacked Rotor Configurations," *AIAA Scitech 2019 Forum*, San Diego, California, 2019, pp. 1–20. doi:10.2514/6.2019-1071, URL `http://arc.aiaa.org`.

[21] Gray, J. S., Hwang, J. T., Martins, J. R. R. A., Moore, K. T., and Naylor, B. A., "OpenMDAO: An open-source framework for multidisciplinary design, analysis, and optimization," *Structural and Multidisciplinary Optimization*, Vol. 59, No. 4, 2019, pp. 1075–1104. doi:10.1007/s00158-019-02211-z.

[22] Kenway, G. K. W., Mader, C. A., He, P., and Martins, J. R. R. A., "Effective Adjoint Approaches for Computational Fluid Dynamics," *Progress in Aerospace Sciences*, Vol. 110, 2019, p. 100542. doi:10.1016/j.paerosci.2019.05.002.

[23] Martins, J. R. R. A., and Ning, A., *Engineering Design Optimization*, Cambridge University Press, 2021. URL `https://mdobook.github.io`.

[24] Falck, R. D., Ingraham, D., and Aretskin-Hariton, E., *Multidisciplinary Optimization of Urban-Air-Mobility Class Aircraft Trajectories with Acoustic Constraints*, 2018. doi:10.2514/6.2018-4985, URL `https://arc.aiaa.org/doi/abs/10.2514/6.2018-4985`.

[25] Hendricks, E. S., Falck, R. D., Gray, J. S., Aretskin-Hariton, E. D., Ingraham, D. J., CHapman, J. W., Schnulo, S. L., Chin, J. C., Jasa, J. P., and Bergeson, J. D., "Multidisciplinary Optimization of a Turboelectric Tiltwing Urban Air Mobility Aircraft," *AIAA/ISSMO Multidisciplinary Analysis and Optimization Conference*, Dallas, TX, 2019.

[26] Hendricks, E. S., Aretskin-Hariton, E., Ingraham, D., Gray, J. S., Schnulo, S. L., Chin, J., Falck, R., and Hall, D., "Multidisciplinary Optimization of an Electric Quadrotor Urban Air Mobility Aircraft," *AIAA Aviation 2020 Forum*, AIAA AVIATION Forum, Virtual Event, 2020, pp. 1–25. doi:10.2514/6.2020-3176.

[27] Ingraham, D., Gray, J., and Lopes, L. V., "Gradient-Based Propeller Optimization with Acoustic Constraints," *AIAA Scitech 2019 Forum*, 2019, pp. 1–12. doi:10.2514/6.2019-1219.

[28] Ingraham, D., Falck, R., and Gray, J. S., "Blade and Trajectory Optimization of a Propeller -Driven Electric Aircraft with Acoustic Constraints," *AIAA Aviation Forum*, Virtual Event, 2020, pp. 1–28. doi:10.2514/6.2020-3141.

[29] Lambe, A. B., and Martins, J. R. R. A., "Extensions to the Design Structure Matrix for the Description of Multidisciplinary Design, Analysis, and Optimization Processes," *Structural and Multidisciplinary Optimization*, Vol. 46, 2012, pp. 273–284. doi:10.1007/s00158-012-0763-y.

[30] Beard, R. W., and McLain, T. W., *Small Unmanned Aircraft: Theory and Practice*, Princeton University Press, 2012.

[31] Brent, R. P., *Algorithms for Minimization without Derivatives*, Prentice-Hall, Englewood Cliffs, NJ, 1973.

[32] Akima, H., "A new method of interpolation and smooth curve fitting based on local procedures," *Journal of the ACM*, Vol. 4, No. 17, 1970, pp. 589–602.

[33] Schmitz, F. H., and Yu, Y. H., "Helicopter Impulsive Noise: Theoretical and Experimental Status," Tech. rep., NASA Ames Research Center, Moffett Field, California, 1983.

[34] Chia, M. H., Duraisamy, K., Padthe, A. K., and Friedmann, P. P., "Active and Passive Helicopter Noise Reduction Using the AVINOR/HELINOIR Code Suite," *Journal of Aircraft*, Vol. 55, No. 2, 2018, pp. 727 – 740. doi:10.2514/1.C034519, URL `www.aiaa.org/randp.`

[35] Lyu, Z., Xu, Z., and Martins, J. R. R. A., "Benchmarking Optimization Algorithms for Wing Aerodynamic Design Optimization," *Proceedings of the 8th International Conference on Computational Fluid Dynamics*, Chengdu, Sichuan, China, 2014. ICCFD8-2014-0203.

[36] Martins, J. R. R. A., Sturdza, P., and Alonso, J. J., "The Complex-Step Derivative Approximation," *ACM Transactions on Mathematical Software*, Vol. 29, No. 3, 2003, pp. 245–262. doi:10.1145/838250.838251.

[37] Mader, C. A., Martins, J. R. R. A., Alonso, J. J., and van der Weide, E., "ADjoint: An Approach for the Rapid Development of Discrete Adjoint Solvers," *AIAA Journal*, Vol. 46, No. 4, 2008, pp. 863–873. doi:10.2514/1.29123.

[38] Martins, J. R. R. A., and Hwang, J. T., "Review and Unification of Methods for Computing Derivatives of Multidisciplinary Computational Models," *AIAA Journal*, Vol. 51, No. 11, 2013, pp. 2582–2599. doi:10.2514/1.J052184.

[39] Hwang, J. T., and Martins, J. R. R. A., "A computational architecture for coupling heterogeneous numerical models and computing coupled derivatives," *ACM Transactions on Mathematical Software*, Vol. 44, No. 4, 2018, p. Article 37. doi:10.1145/3182393.

[40] Hascoet, L., and Pascual, V., "The Tapenade automatic differentiation tool: Principles, model, and specification," *ACM Transactions on Mathematical Software*, Vol. 39, No. 3, 2013, pp. 20:1–20:43. doi:10.1145/2450153.2450158.

[41] Harris, C. R., Millman, K. J., van der Walt, S. J., Gommers, R., Virtanen, P., Cournapeau, D., Wieser, E., Taylor, J., Berg, S., Smith, N. J., Kern, R., Picus, M., Hoyer, S., van Kerkwijk, M. H., Brett, M., Haldane, A., del Río, J., Wiebe, M., Peterson, P., Gérard-Marchant, P., Sheppard, K., Reddy, T., Weckesser, W., Abbasi, H., Gohlke, C., and Oliphant, T. E., "Array programming with {NumPy}," *Nature*, Vol. 585, 2020, pp. 357–362. doi:10.1038/s41586-020-2649-2.

[42] Peterson, P., "F2PY: A Tool for Connecting Fortran and Python Programs," *International Journal of Computational Science and Engineering*, Vol. 4, No. 4, 2009, pp. 296–305. doi:10.1504/IJCSE.2009.029165.

[43] Kermode, J. R., "f90wrap: an automated tool for constructing deep Python interfaces to modern Fortran codes," *J. Phys. Condens. Matter*, 2020. doi:10.1088/1361-648X/ab82d2.

[44] Kitaplioglu, C., Caradonna, F. X., and Mccluer, M., "An Experimental Study of Parallel Blade-Vortex Interaction Aerodynamics and Acoustics Utilizing an Independently Generated Vortex," Tech. rep., Ames Research Center, 1999. URL http://www.sti.nasa.gov.

[45] Beddoes, T. S., "Practical Computation of Unsteady Lift," *Eighth European Rotorcraft Forum*, Association Aeronautique et Astronautique de France, Aix-En-Provence, France, 1982.

[46] Jones, R. T., "The Unsteady Lift of a Wing of Finite Aspect Ratio," Tech. rep., NASA Langley Memorial Aeronautical Laboratory, Langley Field, VA, 1940. URL http://hdl.handle.net/2060/19760011982.

[47] Diaz, P. V., and Yoon, S., "Computational study of nasa's quadrotor urban air taxi concept," *AIAA Scitech 2020 Forum*, Vol. 1 PartF, 2020, pp. 1–21. doi:10.2514/6.2020-0302.

[48] Jia, Z., and Lee, S., "Acoustic analysis of Urban air mobility quadrotor aircraft," *International Powered Lift Conference 2020, IPLC 2020, Held at Transformative Vertical Flight 2020*, 2020, pp. 24–40.

[49] Drela, M., "XFOIL: An Analysis and Design System for Low Reynolds Number Airfoils," *Low Reynolds Number Aerodynamics*, edited by T. J. Mueller, Springer Berlin Heidelberg, Berlin, Heidelberg, 1989, pp. 1–12. doi:10.1007/978-3-642-84010-4_1.

[50] Kreisselmeier, G., and Steinhauser, R., "Systematic Control Design by Optimizing a Vector Performance Index," *International Federation of Active Controls Symposium on Computer-Aided Design of Control Systems, Zurich, Switzerland*, 1979. doi:10.1016/S1474-6670(17)65584-8.

[51] Virtanen, P., Gommers, R., Oliphant, T. E., Haberland, M., Reddy, T., Cournapeau, D., Burovski, E., Peterson, P., Weckesser, W., Bright, J., van der Walt, S. J., Brett, M., Wilson, J., Millman, K. J., Mayorov, N., Nelson, A. R. J., Jones, E., Kern, R., Larson, E., Carey, C. J., Polat, b., Feng, Y., Moore, E. W., VanderPlas, J., Laxalde, D., Perktold, J., Cimrman, R., Henriksen, I., Quintero, E. A., Harris, C. R., Archibald, A. M., Ribeiro, A. H., Pedregosa, F., van Mulbregt, P., and SciPy 1.0 Contributors, "SciPy 1.0: Fundamental Algorithms for Scientific Computing in Python," *Nature Methods*, Vol. 17, 2020, pp. 261–272. doi:10.1038/s41592-019-0686-2.

[52] Wu, N., Kenway, G., Mader, C. A., Jasa, J., and Martins, J. R. R. A., "pyOptSparse: A Python framework for large-scale constrained nonlinear optimization of sparse systems," *Journal of Open Source Software*, Vol. 5, No. 54, 2020, p. 2564. doi:10.21105/joss.02564.